Mid-Fidelity Lattice-Boltzmann Simulations of Proprotor–Wing Aerodynamic Interactions

Alex Natelson Graduate Research Assistant
Duncan Waanders Doctoral Candidate
Shreyas Ashok Doctoral Candidate
Juergen Rauleder Assistant Professor

Daniel Guggenheim School of Aerospace Engineering
Georgia Institute of Technology
Atlanta, Georgia, USA

ABSTRACT

This study investigates the capability of quick turnaround mid-fidelity Lattice-Boltzmann Method (LBM) simulations to resolve complex aerodynamic interactions between proprotors and wings in tiltrotor configurations. A GPU-accelerated LBM solver was coupled with an actuator line model to capture proprotor-induced effects across a range of proprotor tilt angles. An explicit power-law wall model was developed and integrated into the LBM framework to provide near-wall treatment based on velocity profile assumptions. This approach was evaluated in parallel with a no-slip immersed boundary formulation, which does not constitute a wall model but only enforces a no-slip condition at the body surface. Simulation results obtained using both boundary treatments were compared against experimental measurements and high-fidelity CFD data for validation. The power-law model demonstrated good agreement with reference data for drag and it predicted complex flow field phenomena correctly, but exhibited discrepancies in wing lift and pressure distributions at high prop tilt angles, highlighting limitations in capturing complex proprotor wake-induced flow separation. The no-slip immersed boundary model overpredicted drag and exhibited excessive flow separation, limiting its applicability to this flow problem, at least at the investigated spatial resolution. The findings highlight the promise of the LBM as an efficient simulation method for quick-turnaround design and analysis of proprotor–wing interactions, including the transition (or conversion) maneuver, while identifying areas for improvement in the explicit power-law wall model to enable more accurate prediction of separated flows and near-wall behavior.

NOMENCLATURE

a	Speed of sound, $\mathrm{m\,s^{-1}}$
A	Proprotor disk area, πR^2, $\mathrm{m^2}$
AR	Wing aspect ratio, $\frac{b^2}{S}$
b	Wing span, m
c	Wing chord, m
c_l	Lattice speed of sound
C_D	Wing drag coefficient, $\frac{D}{q_\infty S}$
$\boldsymbol{c_i}$	lattice-Boltzmann discretized velocity
C_L	Wing lift coefficient, $\frac{L}{q_\infty S}$
C_p	Wing surface pressure coefficient, $\frac{p-p_\infty}{q_\infty}$
C_T	Proprotor thrust coefficient, $\frac{\pi^3}{4}\frac{T}{\rho_\infty A[\frac{2\pi}{60}\Omega R]^2}$
C_Q	Proprotor torque coefficient, $\frac{\pi^3}{8}\frac{Q}{\rho_\infty A[\frac{2\pi}{60}\Omega R]^2 R}$
D	Wing Drag force, N
f_i	Lattice-Boltzmann population distributions
f_i^{eq}	Lattice-Boltzmann equilibrium population distributions
f_i^*	Multiple-relaxation time collision operator
L	Wing Lift force, N
M_∞	Freestream Mach number, $\frac{V_\infty}{a}$
P	Pressure, Pa
p_∞	Freestream static pressure, Pa
q_∞	Freestream dynamic pressure, $\frac{1}{2}\rho_\infty V_\infty^2$, Pa
Q	Proprotor torque, $\mathrm{N\,m}$
R	Proprotor radius, m
S	Wing planform area, bc, $\mathrm{m^2}$
Δt	timestep
T_∞	Freestream static temperature, K
T	Proprotor thrust, N
u	Streamwise velocity, $\mathrm{m\,s^{-1}}$
$\boldsymbol{u}$	Lattice-Boltzmann macroscopic velocity
u^+	Streamwise velocity nondimensionalized in wall units
u_τ	Friction velocity
v	Spanwise velocity, $\mathrm{m\,s^{-1}}$
V_∞	Freestream velocity, $\mathrm{m\,s^{-1}}$
w_i	Lattice-Boltzmann discretized lattice weights
Δx	Lattice cell width
x	Wing chordwise coordinate, origin at wing leading edge at $\alpha = 0°$, positive downstream parallel to the wind tunnel test section, m
y^+	Wall-normal distance nondimensionalized in wall units
y	Wing chord normal coordinate, origin at wing chord at $\alpha = 0°$, positive perpendicular to freestream velocity, m
z	Wing spanwise coordinate, origin at wing midspan, positive towards wind tunnel test section ceiling, m
α	Wing angle of attack, $°$
ρ	Air density, $\mathrm{kg\,m^{-3}}$
θ	Proprotor tilt angle, degrees
τ	Lattice-Boltzmann relaxation time
τ_w	Wall shear stress
ν	Air kinematic viscosity, $\mathrm{m^2\,s^{-1}}$

Ω Proprotor rotational speed, RPM

INTRODUCTION

Aircraft which combine vertical takeoff and landing (VTOL) capabilities with high-speed conventional cruise performance expand operational possibilities across a range of civilian and military domains. As seen in novel urban/advanced air mobility (UAM/AAM) and tiltrotor (e.g., V-22, XV-15) designs, these aircraft often employ a combination of tilting proprotors for VTOL capabilities and fixed-wing lifting surfaces for efficient cruise. For accurate predictions of flight performance, aerodynamic characteristics, and their implications on flight dynamics and safety, the aerodynamic interactions between the proprotors and wings must be captured. However, these interactions are not yet fully understood, especially in the tiltrotor transition regime. This regime is of particular interest due to the complex aerodynamic interactions that arise between the downwash of the proprotor and the force distribution over the aircraft wings. Those interactions lead to complex flow separation and reattachment phenomena that directly impact the vehicle performance and handling characteristics.

Computational Fluid Dynamics (CFD) provides an effective means of modeling these aerodynamic interactions. Prior studies have demonstrated the applicability of CFD to proprotor–wing interaction problems, including the work of Sugawara and Tanabe (Ref. 1), who established that CFD can reliably capture these dynamic interactions. Subsequent investigations have further reinforced the efficacy of CFD for proprotor–body interaction analysis. For instance, Renaud et al. (Ref. 2) employed high-fidelity CFD methodologies to resolve the aerodynamic interactions between a helicopter rotor and fuselage, capturing key flow phenomena with high accuracy. Similarly, Costes et al. (Ref. 3) highlighted significant advancements in rotorcraft CFD capabilities, particularly in their discussion of the modeling strategies utilized at ONERA.

CFD serves as a powerful tool for analyzing complex aerodynamic interactions, particularly those dominated by viscous effects and turbulence. Accurate resolution of such flow phenomena relies heavily on the use of turbulence modeling. Foundational work by Wilcox (Ref. 4) established the theoretical basis for many widely used turbulence models, forming the cornerstone of modern Reynolds-Averaged Navier–Stokes (RANS) approaches. Subsequent studies by Zhai et al. (Ref. 5) and Zhang et al. (Ref. 6) evaluated the comparative performance of several turbulence closure models, providing insight into their predictive accuracy. Additionally, Aubin et al. (Ref. 7) assessed the fidelity of turbulence models in simulating turbulent flows within water tanks, further validating their applicability in confined, wall-bounded domains.

An additional challenge associated with CFD is the generation of high-quality computational grids. Complex geometries, such as those involving rotorcraft or internal flow configurations, often do not conform easily to structured Cartesian meshes. To address this, a number of advanced grid generation strategies have been developed. Pioneering contributions by Thompson (Ref. 8) offered comprehensive analysis of structured and unstructured mesh generation techniques. Hernandez-Perez et al. (Ref. 9) conducted a focused study on grid generation for simulating internal flow in circular pipes, identifying key meshing constraints and solution sensitivity. Samareh (Ref. 10) further examined the state of CFD grid generation in the context of design and optimization workflows, emphasizing the importance of mesh quality, adaptability, and automation in engineering applications.

Beyond rotorcraft applications, CFD has long been established as a reliable approach for resolving aerodynamic flows over conventional 3D wings. Kulshreshtha et al. (Ref. 11) utilized the ANSYS Fluent solver to investigate flow characteristics over various NACA airfoils. Moreover, the versatility of CFD extends to non-conventional wing configurations, as exemplified by Suresh et al. (Ref. 12), who conducted a comprehensive aerodynamic analysis of a non-planar C-wing configuration. The utility of CFD further encompasses unmanned aerial vehicle (UAV) performance evaluation, as illustrated in the work of Priscariu (Ref. 13), where flow simulations were conducted to model the aerodynamic behavior of a UAV flying wing configuration.

CFD has also been extensively employed in the simulation of rotor aerodynamics and their wake interactions. Kasmaiee et al. (Ref. 14) utilized CFD to examine rotor blade performance under various unsteady wind conditions, demonstrating the capability of CFD to capture complex transient aerodynamic phenomena. Similarly, Song and Perot (Ref. 15) applied CFD to investigate the flow characteristics around the blades of a wind turbine, further exemplifying the versatility of CFD in rotor-based applications. In related work, Yeo et al. (Ref. 16) performed a structural loads analysis of the ONERA 7A rotor using the high-fidelity CFD frameworks elsA/HOST and Helios/RCAS to evaluate their predictive capabilities and accuracy. Of particular relevance to the present study is the application of CFD to rotor wake modeling. Bechmann et al. (Ref. 17) conducted modeling with CFD to examine wind turbine wake dynamics and validated their results against experimental measurements, reinforcing the credibility of CFD for rotor wake analyses. Furthermore, Cao et al. (Ref. 18) developed a CFD optimization tool for rotors that incorporated wake effects into wind turbine rotor design, highlighting the emphasis within the rotorcraft community on accurately capturing wake effects. These prior efforts underscore the effectiveness of CFD when applied to rotor wake-resolved simulations.

Extensive experimental research has been conducted to investigate rotor aerodynamics and wake interaction phenomena. A foundational study by Felker and Light (Ref. 19) systematically characterized the influence of rotor and wing geometric variations on rotor–wing aerodynamic interactions in hover. More recently, Chen and Rauleder (Ref. 20) executed a comprehensive experimental campaign to examine the unsteady aerodynamic loading induced by rotor wakes impinging on a ship deck. Their methodology combined load cell measurements, Particle Image Velocimetry (PIV) sweeps, and distributed pressure sensing to capture both transient and spatially resolved flow features.

Further expanding on rotor–wing interaction studies, Sridhar et al. (Ref. 21) performed a series of experimental measurements across a range of proprotor tilt angles, encompassing the hover, transition, and cruise regimes representative of tiltrotor operation. Their experimental setup employed independent force measurements on both the rotor and wing using load cells, along with surface pressure sensors and PIV imaging to resolve the coupled flow fields. In parallel, high-fidelity unsteady Reynolds-Averaged Navier–Stokes (URANS) CFD simulations were performed to complement and validate the experimental data.

While these high-fidelity CFD approaches offer detailed and accurate predictions of unsteady aerodynamic interactions, they are computationally demanding, often requiring days to weeks of runtime on high-performance computing (HPC) infrastructure. Such computational expense renders them impractical for time-sensitive applications such as vehicle design iteration, flight envelope mapping, or real-time performance assessment. Consequently, there is a growing need for low- and mid-fidelity modeling techniques that can deliver significantly reduced turnaround times while maintaining sufficient accuracy. However, the effectiveness of these reduced-order approaches in capturing the highly nonlinear and coupled aerodynamic phenomena characteristic of proprotor–wing interactions remains an open question and a central motivation for the present study.

The Lattice-Boltzmann Method (LBM) is one candidate methodology for simulating and modeling complex aerodynamic flows, particularly those characterized as weakly compressible. Unlike traditional Navier–Stokes solvers, the LBM operates by solving the discretized Lattice-Boltzmann equation on a Cartesian lattice structure. Through a Chapman-Enskog expansion, the LBM can be demonstrated to recover the macroscopic Navier–Stokes equations, as shown by Krüger (Ref. 22). A key advantage of the LBM is its highly parallelizable structure which enables it to be run efficiently on graphical processing units (GPUs). This parallelism allows for high computational efficiency, which enables modeling of complex flows at significantly reduced computational cost compared to traditional high-fidelity CFD methods.

Over the past several decades, considerable research has been devoted to improving the performance and expanding the applicability of the LBM. Notably, Körner et al. (Ref. 23) made foundational contributions by investigating strategies for parallelization of LBM algorithms, increasing computational efficiency, and laying the ground work for its use in large-scale simulations. Building on this, Kuznik et al. (Ref. 24) pioneered GPU-accelerated implementations of the LBM, allowing it to be comparable to CFD codes operating on high-performance computing clusters. These advances have since been adopted and extended by numerous researchers. For example, Wang et al. (Ref. 25) utilized the LBM to perform simulations of turbulent flows around urban structures, further validating the method's capability for resolving complex aerodynamic environments.

Given the focus of the present study on aerodynamic interactions with lifting surfaces, accurate modeling of wall-bounded flow behavior is essential. However, the use of Cartesian grids inherent to the LBM poses significant challenges for near-wall resolution. In particular, achieving grid resolutions sufficient to maintain a non-dimensional wall distance of $y^+ \approx 1$, a requirement for fully-resolved boundary layers, is computationally prohibitive in most practical scenarios. To address this limitation, wall stress models are employed to approximate the effects of the near-wall flow without explicitly resolving the viscous sub-layer. A broad range of boundary condition formulations and wall models have been developed for both traditional CFD methodologies and LBM frameworks. One such treatment was developed by Mei et al. (Ref. 26), where they spearheaded the design and implementation of an "accurate" curved boundary treatment specifically for the LBM, addressing the challenges associated with non-Cartesian geometries. Dorschner et al. (Ref. 27) developed an immersed no-slip boundary condition, which was later applied by Ashok and Rauleder (Ref. 28) in simulations of both static and translating ship geometries to investigate ship airwake behavior. Furthermore, Wissocq et al. (Ref. 29) extended the applicability of the LBM to high Reynolds number flows by adapting characteristic boundary conditions, enhancing accuracy and stability in that challenging aerodynamic regime.

Boundary condition strategies for complex and dynamic geometries have also been the subject of significant research. Kurban et al. (Ref. 30) employed a combination of slip and bounce-back boundary conditions in their study of ship airwake aerodynamics, demonstrating strong correlation between experimental measurements and the LBM predictions. Similarly, Wang et al. (Ref. 31) developed an immersed moving boundary condition for the LBM, enabling accurate modeling of bodies in relative motion. Ashok and Rauleder (Ref. 28) employed a similar immersed moving boundary condition in the LBM simulation Aslan et al. (Ref. 32) conducted a comparative assessment of various curved boundary treatments for the LBM, concluding that multiple approaches yielded near-identical aerodynamic predictions, thereby offering flexibility in boundary modeling choices.

Beyond accurate surface modeling, a significant computational challenge in rotor aerodynamics lies in the accurate yet efficient numerical representation of rotating blades. One common approach involves explicitly resolving individual rotor blades using highly refined body-fitted grids in conjunction with high-order numerical schemes to accurately capture unsteady aerodynamic phenomena. This methodology was implemented in the high-fidelity CFD simulations presented by Sridhar et al. (Ref. 21). While this approach guarantees accuracy, it incurs a substantial computational cost, particularly for large-scale or time-resolved simulations. As a computationally efficient alternative, the Actuator Line Method (ALM), originally introduced by Sorensen and Shen (Ref. 33), models each rotor blade as a one-dimensional line along the span. In this formulation, local inflow velocities at discrete blade segments are first extracted from the surrounding flow field. Blade element theory is then applied to compute the aerodynamic forces generated by each segment, which are subsequently projected onto the computational domain at the appropriate physical locations. This methodology enables the discrete aerodynamic influence of individual blades to be incorporated into the simulation without explicitly resolving blade geometry. However, the ALM does not capture viscous effects along the blade surface and generally neglects spanwise flow phenomena that occur in real rotor operation. Despite these limitations, the method offers a favorable balance between computational efficiency and predictive fidelity, making it well-suited for application in the present study.

In recent years, the actuator line method has been widely adopted within the CFD community for a broad range of applications. Apsley et al. (Ref. 34) implemented the ALM to simulate tidal wind turbine flows, demonstrating its effectiveness in capturing blade-induced wake dynamics. Similarly, Baba-Ahmadi and Dong (Ref. 35) conducted a comprehensive validation of the ALM against experimental measurements, confirming its capability to accurately predict rotor performance and wake characteristics. Continued development has led to several enhancements of the ALM to address limitations. Notably, Jha and Schmitz (Ref. 36) introduced modifications to mitigate inaccuracies associated with force projection, improving the physical consistency of the model. Additionally, Churchfield et al. (Ref. 37) proposed an advanced formulation that incorporated corrections to the freestream velocity calculation and refined force projection algorithms, further enhancing model accuracy. These methodological advancements have enabled the ALM to be applied across a broad spectrum of aerodynamic applications with improved computational efficiency and acceptable predictive accuracy.

Significant advancements have also been made in the implementation of the actuator line methodology within the LBM. Asmuth et al. (Ref. 38) conducted a detailed sensitivity and performance analysis of the actuator line model within the LBM, providing valuable insights into its numerical behavior and accuracy. Similarly, Rullaud et al. (Ref. 39) integrated the actuator line approach into the LBM for wind turbine simulations. Furthermore, Grondeau et al. (Ref. 40) employed the actuator line model within the LBM to simulate and analyze the wake dynamics of a ducted tidal turbine, further validating the applicability of this approach for wake-focused simulations. Collectively, these studies establish the actuator line model as a credible and effective technique for rotor modeling within the LBM simulations.

The use of the LBM for rotor–body aerodynamic interaction simulations has been demonstrated in recent years. Bludau et al. (Ref. 41) applied the LBM to model the complex flow field around a helicopter landing on a ship deck, capturing critical wake–deck interactions. Gourdain et al. (Ref. 42) employed the LBM to investigate the wake behavior of an air vehicle operating in ground effect, further validating the LBM's applicability to rotor-induced flow simulations. More recently, Ashok and Rauleder (Ref. 43) demonstrated the use of the LBM for real-time simulations of rotorcraft ship landings, showing strong agreement with wind tunnel measurements. These prior studies underscore the viability of the LBM as an effective computational framework for simulating aerodynamic interactions between rotors and solid surfaces, thus providing a foundation for its application to proprotor–wing interaction analyses in the present work.

The objective of the present study is to assess the capability of a mid-fidelity quick turnaround GPU-accelerated LBM model to resolve aerodynamic interactions between a tilting proprotor and a wing. It is assessed whether mid-fidelity LBM simulations are sufficient for analysis of complex transition (or conversion) regimes of tiltrotor aircraft that include flow separation and reattachment on the wing. The present study adopts the Churchfield advanced actuator line formulation (Ref. 37) for modeling the proprotor, leveraging its capability to accurately capture rotor-induced aerodynamic effects with reduced computational cost. Additionally, the present study employs the explicit power-law wall model developed by Wilhelm et al. (Ref. 44), which offers an efficient approach to modeling near-wall behavior in high Reynolds number flows. For comparison, a no-slip immersed boundary wall treatment (Ref. 27) is also implemented, allowing for a comparison of accuracy between the two boundary conditions. The physical accuracy of the LBM results is evaluated by comparing proprotor and wing loads, wing surface pressure distributions, and flow fields with experimental and high-fidelity CFD data from Ref. 21.

TECHNICAL APPROACH

The Lattice-Boltzmann Method

The LBM is an alternative fluid simulation method which does not solve the conservation equations for mass, momentum, and energy unlike traditional CFD methods. Instead, the LBM models the local fluid dynamics on a mesoscopic scale where the fluid domain is made up of lattice cells. Each lattice cell contains particle distribution functions, or populations, where the number of populations in each cell is defined by the lattice cell configuration being used. The naming convention for the lattice cell configurations is DxQyy, where x represents the number of dimensions, and yy represents the number of populations in each cell. Common cell configurations include D1Q3, D2Q9, D3Q15, D3Q19, and D3Q27. This study utilized the D3Q19 lattice configuration because of its computational efficiency and versatility for a variety of cases. A visual representation of the D3Q19 particle populations is shown in Figure 1.

As the simulation commences, the populations within the lattice cells are reallocated according to the Lattice-Boltzmann equation, shown in Eq. 1.

$$f_i(\boldsymbol{x} + \boldsymbol{c_i}\Delta t, t + \Delta t) = f_i^\star(\boldsymbol{x}, t) \tag{1}$$

The above Eq. 1 was derived from the discretized Boltzmann equation, and it describes the motion of the particle populations as they move to neighboring lattice cells by propagating along their discretized velocities. The multiple-relaxation-time (MRT) collision operator (Ref. 45) was utilized to relax

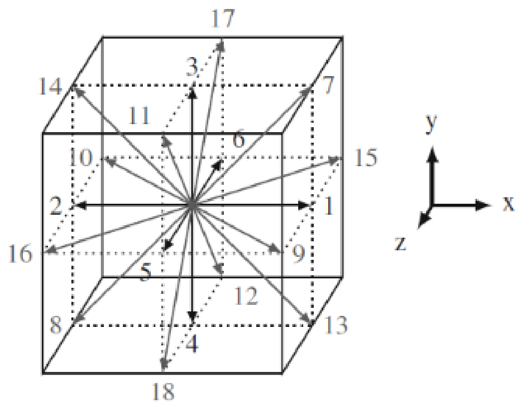

Figure 1: D3Q19 Population Distribution, adapted from Ref. 22.

moments of the cell populations to their equilibrium states and is shown in the following Eq. 2.

$$f_i^*(\mathbf{x},t) = f_i(\mathbf{x},t) - (\mathbf{M^{-1}SM})_{ij}\left[f_j(\mathbf{x},t) - f_j^{eq}(\mathbf{x},t)\right] + \Delta t F_i^* \quad (2)$$

In Eq. 2, $\boldsymbol{M}$ is the moment transformation matrix, $\boldsymbol{S}$ is a diagonal matrix which holds the relaxation rates for each moment, and F' is the discretized forcing term which includes the external forces. A relation between pressure and density can be evaluated in terms of lattice units as defined in Eq. 3 below.

$$P = c_l^2 \cdot \rho \quad (3)$$

The speed of sound of the lattice can be calculated through the following Eq. 4, where Δt is the timestep, and Δx is the length of the edge of the lattice cell.

$$c_l^2 = \frac{1}{3}\frac{\Delta x^2}{\Delta t^2} \quad (4)$$

The below Eqs. 5 and 6 give relations for calculating the lattice density and momentum in lattice units. Those can be converted back to physical units of choice through scaling by a conversion factor.

$$\rho(\boldsymbol{x},t) = \sum_i f_i(\boldsymbol{x},t) \quad (5)$$

$$\rho\boldsymbol{u_l}(\boldsymbol{x},t) = \sum_i \boldsymbol{c}_i f_i(\boldsymbol{x},t) \quad (6)$$

Explicit Power-Law Wall Model

As outlined in the preceding discussion, the wall modeling strategy adopted in this work is the explicit power-law formulation developed by Wilhelm et al. (Ref. 44). The Cartesian grids used in the LBM generally make it infeasible to construct a mesh that can fully resolve the boundary layer (first cell height $y^+ < 1$). Instead, this wall modeling approach models the boundary layer shape based on a given velocity profile, allowing for considerably coarser mesh resolutions at the wing surface.

The application of this model necessitates the reconstruction of macroscopic flow variables, specifically, density, velocity and the stress-tensor, at near-wall locations. This reconstruction is accomplished via interpolation procedures that rely exclusively on fluid nodes located entirely outside of the solid geometry. A notable limitation of this approach arises near complex or sharply curved body surfaces, where the availability of fully fluid nodes in the interpolation stencil is restricted. This limitation can introduce localized inaccuracies in the velocity reconstruction and, consequently, in the wall shear stress estimation. The employed interpolation strategy and its implications are illustrated schematically in Fig. 2.

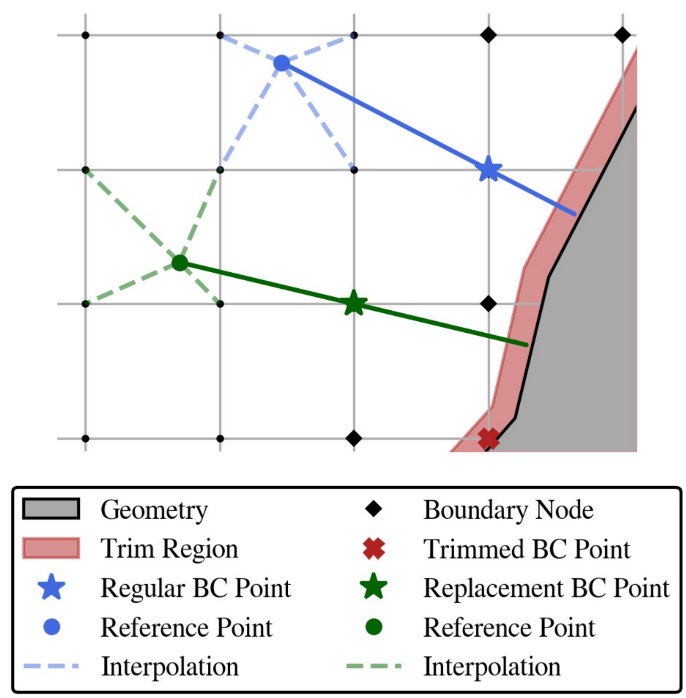

Figure 2: Reference point interpolation and boundary node trimming strategy

To enable interpolation to occur when looking at near-boundary points, a "reference point" is defined at a specified distance from the boundary. This reference point serves as the target location for velocity interpolation from neighboring fluid nodes. In both the present study and the work of Wilhelm et al. (Ref. 44), the reference point was defined at a distance of $2.5\Delta x$ from the wall, measured along the wall-normal vector. This placement is designed to ensure that the reference point lies within a region populated exclusively by fluid nodes, thereby enabling robust interpolation. The selected interpolation methodology for this study is the Inverse Distance Weighting (IDW) approach described by Panigrahi (Ref. 46) and employed by Wilhelm et al. (Ref. 44). The spatial arrangement of the boundary and reference nodes, as well as the associated interpolation region, is depicted in Fig. 2.

As previously mentioned, the explicit power-law model uses a velocity profile to model the shape of the boundary layer. The velocity profile used by Wilhelm et al in their implementation (Ref. 44) is an exponential profile proposed by Prandtl and defined as follows in Eq. 7.

$$u^+ = g(y^+) \rightarrow u^+ = A(y^+)^{\frac{1}{7}} \tag{7}$$

In Eq. 7, A is a coefficient that can depend on the Reynolds number, and the exponent $\frac{1}{7}$ was chosen based on the work done by Werner and Wengle in Large Eddy Simulations (LES) (Ref. 47). The universal rescaled velocity profile and the normalized distance to the wall are defined as follows in Eq. 8.

$$u^+ = \frac{u}{u_\tau}, y^+ = \frac{y u_\tau}{\nu} \tag{8}$$

In Eq. 8, u is the tangential velocity at a distance y from the wall, ν is the fluid's kinematic viscosity, and u_τ is the friction velocity related to the wall shear stress through Eq. 9.

$$\tau_w = \rho u_\tau^2 \tag{9}$$

In Eq. 9, τ_w is the wall shear stress. The velocity can be interpolated at the reference point to get the tangential velocity at the reference point, u_{Ref}. Once u_{Ref} is known, along with the height of the reference point and the original point from the body, the values can be used in the power-law formulation in Eq 10.

$$u(y) = \begin{cases} u_{Ref} \cdot \frac{y}{y_{Ref}}, & \text{if } y^+_{Ref} \leq y^+_c, \\ u_{Ref} \cdot (\frac{y}{y_{Ref}})^B, & \text{if } y^+_{Ref} \geq y^+_c, \end{cases} \tag{10}$$

In Eq. 10, y_{Ref} represents the distance to the boundary from the reference point, y^+_{Ref} represents the same distance nondimensionalized in wall units, $y^+_c = 11.81$ (Ref. 47) represents the normalized height of the viscous sublayer, u_{Ref} is the wall-tangential velocity at the reference point, y is the distance to the boundary from the boundary point, and $B = 1/7$ is the power-law exponent. Using the power-law profile, the desired velocity and velocity gradient are calculated at the boundary point, and the relevant LBM populations are specified using Grad's approximation (Ref. 27). Grad's approximation is given by the following Eq. 11.

$$\begin{aligned} f_i(\rho, u, P) = w_i \Bigg[\rho + \frac{\rho u_\alpha c_{i\alpha}}{c_l^2} \\ + \frac{1}{2c_l^4}(P_{\alpha\beta} - \rho c_l^2 \delta_{\alpha\beta})(c_{i\alpha}c_{i\beta} - c_l^2\delta_{\alpha\beta})\Bigg] \end{aligned} \tag{11}$$

In Eq. 11, ρ is the density, $\mathbf{u}$ is the velocity vector, and $\mathbf{P}$ is the pressure tensor. Additionally, w_i is each lattice direction weight, $\mathbf{c_i}$ indicates each lattice discrete velocity vector, and c_l is the lattice speed of sound.

The explicit power-law wall model was successfully incorporated into the primary LBM architecture for the computation of macroscopic flow variables. However, challenges were encountered in the evaluation of the non-equilibrium terms. In particular, as mesh refinement was increased, a greater number of boundary nodes appeared in close proximity to the model surface. This proximity poses numerical difficulties, as the non-equilibrium distribution functions involve inverse dependence on the distance to the wall, as outlined in the work of Dorschner et al. (Ref. 27). When this distance becomes sufficiently small (e.g., below 0.1 lattice units), the resulting singularity in the denominator induces unbounded values in the distribution function updates, thereby compromising numerical stability and halting the simulation.

To mitigate this issue, a boundary node trimming technique was implemented, following the approach described by Degrigny et al. (Ref. 48). This procedure establishes a threshold distance between a boundary node and the model surface, below which the node is excluded from computation and reclassified as internal to the solid domain. A sensitivity study conducted on trimming distance yielded that the most accurate and stable threshold distance was 0.5 lattice units. Accordingly, this threshold was adopted for all of the LBM simulations presented in this work.

No-Slip Immersed Boundary Wall Treatment

To enable comparative assessment of boundary modeling approaches within the LBM framework, this study incorporates a second wall treatment: the Grad immersed boundary condition, originally developed by Dorschner et al. (Ref. 27). Designed for simulations involving complex, curved, or moving geometries embedded in Cartesian grids, this method reconstructs missing distribution functions at boundary-adjacent lattice nodes through interpolation of macroscopic flow quantities; specifically, velocity, density, and pressure tensor components.

The Grad boundary model imposes the geometry of the solid body onto the Cartesian mesh and enforces a no-slip condition at the immersed surface. It interpolates macroscopic quantities at the boundary and reconstructs distribution functions using a truncated expansion in terms of velocity moments. This approach has previously been applied in simulations of ship-induced air wakes by Ashok and Rauleder (Refs. 28,43), demonstrating its flexibility in handling dynamically evolving geometries. The boundary point trimming strategy introduced earlier and illustrated in Figure 2 was also implemented in conjunction with this boundary model.

This wall treatment employs the same Grad-based approximation previously introduced and defined in Eq. 11. In this case, however, a no-slip condition is explicitly imposed at the wall, in contrast to the explicit power-law wall model, which seeks to model boundary layer behavior. The reconstructed particle distribution functions at boundary nodes are obtained using the truncated moment expansion shown in Eq. 11. In order to calculate the velocity $\mathbf{u}$, the following interpolation scheme in Eq. 12 is used that blends wall and fluid node velocities based on their normalized distance to the wall.

$$u = \frac{1}{n_D} \sum_{i \in D} \frac{q_i u_{f,i} + u_{w,i}}{1 + q_i} \quad (12)$$

Here, $\mathbf{u_{f,i}}$ represents the fluid velocity at the neighboring fluid node, which is $\mathbf{x} + \mathbf{c_i}$. The wall velocity is represented by $\mathbf{u_{w,i}}$ and q_i is the non-dimensional distance to the wall along a given lattice direction. The fluid density at the boundary node is reconstructed via a combination of bounce-back contributions and wall velocity effects, as given by the following Eq. 13.

$$\rho = \rho_{bb} + \sum_{i \in D} 6 w_i \rho_0 c_i \cdot u_{w,i} \quad (13)$$

Eq. 13 uses ρ_0 to represent the system-averaged density and all other variables as previously detailed. The pressure tensor is approximated using both an equilibrium and a non-equilibrium portion as shown in the following Eq. 14.

$$P_{\alpha\beta} = \rho c_s^2 \delta_{\alpha\beta} + \rho u_\alpha u_\beta - \frac{\rho c_s^2}{\omega} \left(\frac{\partial u_\beta}{\partial x_\alpha} + \frac{\partial u_\alpha}{\partial x_\beta} \right) \quad (14)$$

The final term represents the non-equilibrium stress contribution and is evaluated using first-order finite difference approximations of the velocity gradients. Complete formulation details and implementation guidelines for the Grad immersed boundary model can be found in Ref. 27.

Actuator Line Methodology

To simulate the proprotor, a mid-fidelity actuator line method (ALM) is used. ALM simulations allow for significant reductions in simulation cost as compared to meshed-blade simulations used in high-fidelity CFD studies. The ALM represents individual rotor blades as lines with a discretized number of radial stations along the blade aerodynamic center. At each station, the aerodynamic forces are calculated and applied as source terms to the surrounding fluid grid points.

The present implementation uses the approach of Churchfield et al. (Ref. 37), where the forces are applied using a non-isotropic Gausian projection as desribed in Equation 15. This is done to better match the force distribution of the underlying airfoil sections. This is achieved by scaling proportionally to the blade chord, thickness, and radius (denoted by the subscripts c,t and r respectively) in the corresponding directions.

$$g(x_c, x_t, x_r) = \frac{1}{\epsilon_c \epsilon_t \epsilon_r \pi^{\frac{3}{2}}} \exp\left(-\frac{(x_c - x_{c,0})^2}{\epsilon_c^2} - \frac{(x_t - x_{t,0})^2}{\epsilon_t^2} - \frac{(x_r - x_{r,0})^2}{\epsilon_r^2} \right) \quad (15)$$

The forces at each radial station are based upon blade-element theory (BET) calculations that use the local inflow velocities at each station. These velocities are obtained through spatial sampling of the surrounding flow field at discrete sensor points arranged in a circular ring about the radial station. In the present study, the inflow velocity is averaged from a ring consisting of 20 sensor points.

Fig. 3 depicts the sensor locations and nonisotropic Gaussian force projection scheme. A similar actuator line approach has been previously used in the Reduced Order Aerodynamic Model (ROAM) (Ref. 49), available in the CREATE™-AV Helios rotorcraft simulation suite.

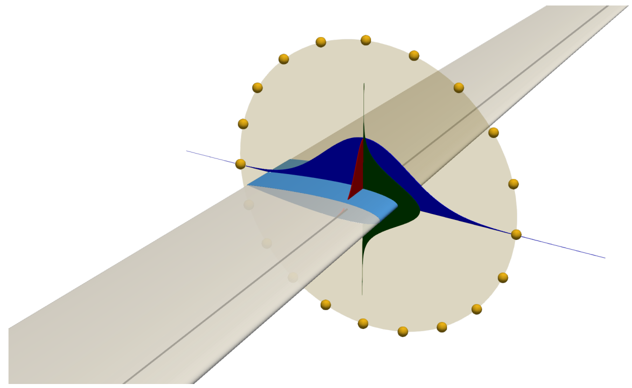

Figure 3: Representative actuator line radial station (light blue) with surrounding inflow sensor locations (yellow) and 3D nonisotropic Gaussian projection scaling distributions for each axis (dark blue, red, green).

Test Conditions

The primary objective of this study is to assess and compare the performance of different boundary modeling approaches within the Lattice-Boltzmann method (LBM) framework for simulating complex proprotor–wing aerodynamic interactions. To facilitate this comparison, simulation results are benchmarked against the experimental and high-fidelity CFD data presented by Sridhar et al. (Ref. 21), which evaluated tiltrotor–wing interactions under controlled conditions. The present modeling setup replicates the test parameters described in Ref. 21 and shown in Table 1, ensuring a consistent basis for validation and analysis.

To represent the XV-15 tiltrotor wing, a rectangular, untwisted wing with a span of $b = 1.52$m, chord length $c = 0.25$m, and $AR = 6.13$ was positioned centrally within the computational domain. The airfoil profile was selected as a NACA 0023 section, maintaining the thickness characteristics of the XV-15 while eliminating camber-induced effects. A two-bladed proprotor with a radius of $R = 0.19$m was used, corresponding to one-third of the full-scale radius-to-chord ratio of the XV-15 configuration and consistent with the reduced-scale geometry employed by Sridhar et al. (Ref. 21). The proprotor hub was offset by a distance of 0.98c from the 0.3c spanwise spar location, about which it rotated. A temporal resolution of $\Delta t = 3.0 \cdot 10^{-5}$s (30 microseconds) was used throughout. Aerodynamic loads were recorded at every simulation timestep, while surface pressure data was sampled at a frequency of 1000Hz, and flow field visualizations were stored

Table 1: Operational Conditions and LBM Simulation Parameters

Parameter	Metric
Wingspan (S) (m)	1.52
Wing Chord (m)	0.25
Domain Size	4S × 1.5S × 2.5S
Static Pressure (p_∞)	96,800 Pa
Static Temperature (T_∞)	295.65 K
Fluid Density (ρ_∞)	1.141 kg/m^3
Reynolds Number	1.03 million
Smagorinsky Constant	0.042
Proprotor Tilt Angle (θ)	$0°, 15°, 30°, 45°, 60°, 75°, 90°$
Freestream Velocity (V_∞)	10 m/s
Proprotor Rotational Speed (Ω)	7000 RPM
Geometry	With Proprotor Without Proprotor
Boundary Condition	Explicit Power-Law Wall Model No-Slip Immersed Boundary
Isolated Wing Simulation Time	1.0 s
Isolated Wing Initialization Period	t = 0.0 s to t = 0.5 s
Isolated Wing Data Collection Period	t = 0.5 s to t = 1.0 s
Proprotor and Wing Simulation Time	0.6 s
Proprotor and Wing Initialization Period	t = 0.0 s to t = 0.3 s
Proprotor and Wing Data Collection Period	t = 0.3 s to t = 0.6 s

at a frequency of 66Hz. For load and pressure analysis, time-averaging was performed over the latter half of each simulation to ensure statistical convergence. The resulting averaged values are compared with experimental and CFD datasets in the Results section.

The high-fidelity CFD simulations presented by Sridhar et al. (Ref. 21) were carried out using the multidisciplinary rotorcraft simulation suite CREATE™-AV Helios (Ref. 50). This solver employs body-fitted structured grids for resolving near-body flow features, which are coupled with a Cartesian-based off-body solver. In Ref. 21, the near-body solution was resolved using the OVERFLOW solver (Ref. 51), while the off-body grid solution was handled by SAMCart (Refs. 50, 52). The mesh used for these simulations comprised approximately 24.9 million computational cells, offering high spatial resolution for both rotor and wing flow structures.

A notable difference between the present study and the reference simulations lies in the treatment of the proprotor support structure. In the experimental and OVERFLOW CFD setups of Sridhar et al. (Ref. 21), a physical support strut was included, as shown in Figure 4. Due to the current structure of the implemented LBM refinement hierarchy, which prohibits solid bodies from intersecting multiple refinement levels, inclusion of the support strut would necessitate a substantial expansion of the finest mesh level. Given available memory limitations, such an expansion would necessitate a reduction in spatial resolution around the wing, thereby degrading fidelity in the region of primary aerodynamic interest. Consequently, the current study omits the proprotor support structure and instead focuses exclusively on the wing–proprotor system. This approach enables a baseline evaluation of the accuracy achievable by the LBM with respect to fundamental aerodynamic interactions in the absence of additional geometric complexity.

A visualization of the full computational domain and its associated refinement hierarchy is presented in Figure 5. In this

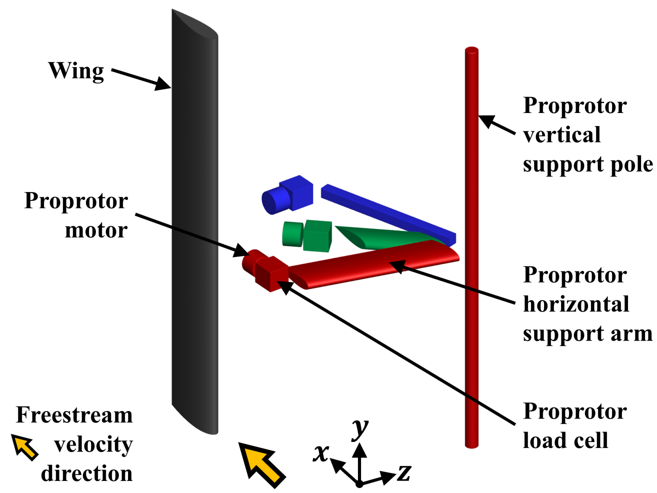

Figure 4: Proprotor support structure used in high-fidelity CFD results from Ref. 21, for proprotor tilt angles of $\theta = 0°$ (red), $\theta = 45°$ (green), and $\theta = 90°$ (blue). Reproduced from Ref. 21

figure, the dark red region denotes the finest resolution level, within which the wing model, shown in dark green, is embedded. The adjacent orange region corresponds to the refinement level containing the rotor, which is indicated in blue. Each successive refinement level exhibits a cell size that is doubled in each spatial direction relative to the finer level it encloses. The coarsest grid, indicated in dark blue, has cells that are 16 times larger in each direction than those in the finest grid region.

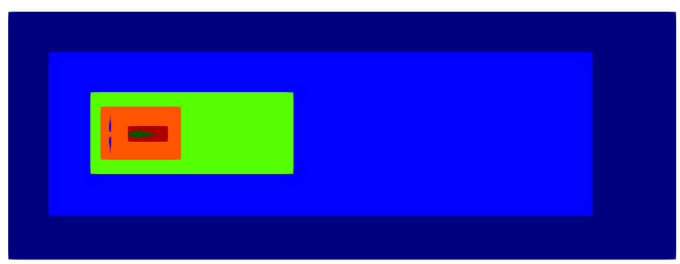

Figure 5: Selected LBM computational domain for all cases, rotor position shown corresponds to proprotor tilt angle of $\theta = 0°$

The computational domain size and resolution for the LBM simulations was determined through a resolution sensitivity study to ensure adequate fidelity in resolving near-body and wake flow features. The final domain configuration consisted of five nested grid refinement levels, with the wing situated within the finest level and the proprotor positioned in the immediately coarser region above. The finest grid level provided a resolution of 2000 cells per wingspan, corresponding to approximately 326 cells along the chordwise direction. This resolution yielded a non-dimensional wall distance of approximately $y^+ \approx 25$, suitable for wall-modeled turbulent boundary layers. The total domain comprised approximately 600 million computational cells. At this resolution, each proprotor–wing case required approximately 100 minutes to fully simulate on eight NVIDIA A100 GPUs. The isolated wing cases required approximately 230 minutes to fully run on eight NVIDIA A100 GPUs due to their increased simulation time.

RESULTS AND DISCUSSION

Flow Fields and Wing Surface Pressure Distributions

This section presents a comparative analysis of flow visualizations and pressure distributions from the LBM simulations against the experimental and high-fidelity OVERFLOW CFD results reported by Sridhar et al. (Ref. 21). The proprotor tilt angles selected for discussion represent key configurations within the transition flight regime: 0°, 45°, and 90°. All flow fields are compared in a cross-sectional plane located at y=0.5R, and surface pressures are compared in a plane at y=-0.5R from the midspan of the wing.

The first flow field comparison, shown in Figure 7, corresponded to a proprotor tilt angle of 0° which represents a forward-flight condition for tiltrotor configurations. At this condition, several notable similarities and differences emerged between the two LBM boundary conditions and the reference experimental and CFD datasets. The LBM power-law wall model exhibited high-velocity regions above and below the wing that closely matched those in the experimental and high-fidelity OVERFLOW CFD results. Moreover, the vortex structures near the lateral extents of the wake ($\approx \pm 0.5\ z/c$) are well captured in the LBM power-law flow field, demonstrating strong qualitative agreement with the reference data. Given this close alignment in the flow visualizations, the discrepancy observed in the integrated aerodynamic loads is notable. Since the computed load coefficients are inherently three-dimensional, they represent integrated contributions across the entire wingspan. This discrepancy implies that inaccuracies in flow resolution may be present in outboard regions of the wing, beyond the primary influence of the proprotor wake. Addressing these areas represents an important direction for future refinement.

The LBM no-slip immersed boundary condition also captured high-velocity regions near the wing surface; however, discrepancies became apparent within the wake region. Specifically, the wake produced by the no-slip immersed condition diverged in shape and location, and the outer-edge vortex structures did not align with those reported in Ref. 21. Across all flow fields, vortex breakdown was observed toward the edges of the wake and downstream near $x/c = 1.5$, indicating a flow feature that is present in all modeling approaches evaluated. Additionally, a stagnation point with low velocity magnitude was visible near the leading edge of the wing in all datasets, further confirming qualitative agreement.

Differences became more pronounced in the separation behavior over the wing. The LBM power-law solution predicted a separation region on the upper surface near the trailing edge, while the no-slip immersed boundary condition resulted in extensive separation on both the upper and lower surfaces, originating near the quarter-chord position. Interestingly, a small separation region was also observed near the trailing edge in the high-fidelity CFD simulation; however, the experimental flow field exhibited no visible separation over the wing surface. This discrepancy indicates a tendency for both LBM boundary conditions to underpredict skin friction, leading to early flow separation, which was more pronounced in the no-slip immersed boundary formulation.

Figure 6 compares the surface pressure coefficient (C_p) distributions obtained from the LBM simulations against high-fidelity OVERFLOW CFD results at a spanwise station of $y = 0.5R$ and a proprotor tilt angle of 0°. Several physically relevant trends emerged from this comparison. Notably, the upper surface pressure distributions shown in Figure 6a demonstrated strong agreement between both LBM boundary conditions and the high-fidelity data reported by Srivathsan et al. (Ref. 21). While the trends across all datasets were qualitatively consistent, the experimentally measured pressure coefficients were uniformly lower in magnitude than those predicted by both computational approaches.

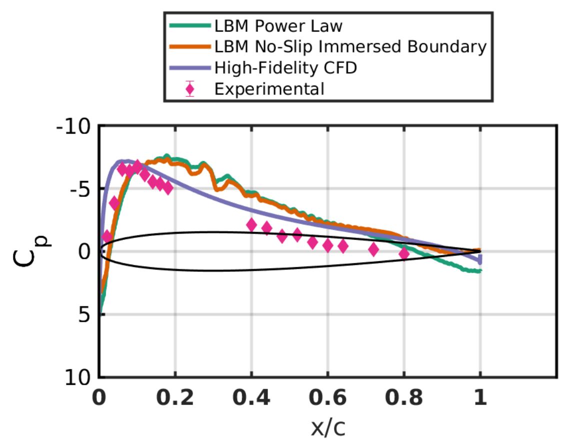

a)

Wing Upper Surface

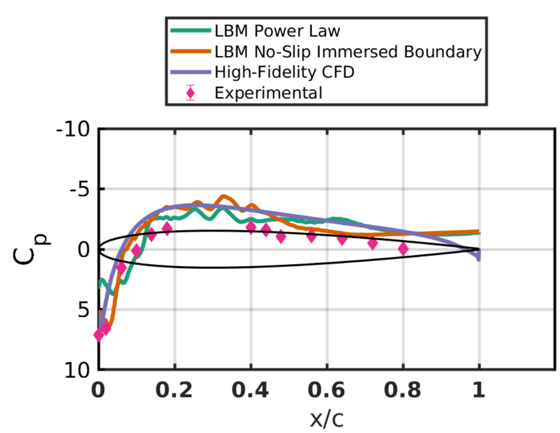

b)

Wing Lower Surface

Figure 6: Pressure coefficient comparison to results from Ref. 21 at $y = -0.5R$ from the wing midspan for $\theta = 0°$.

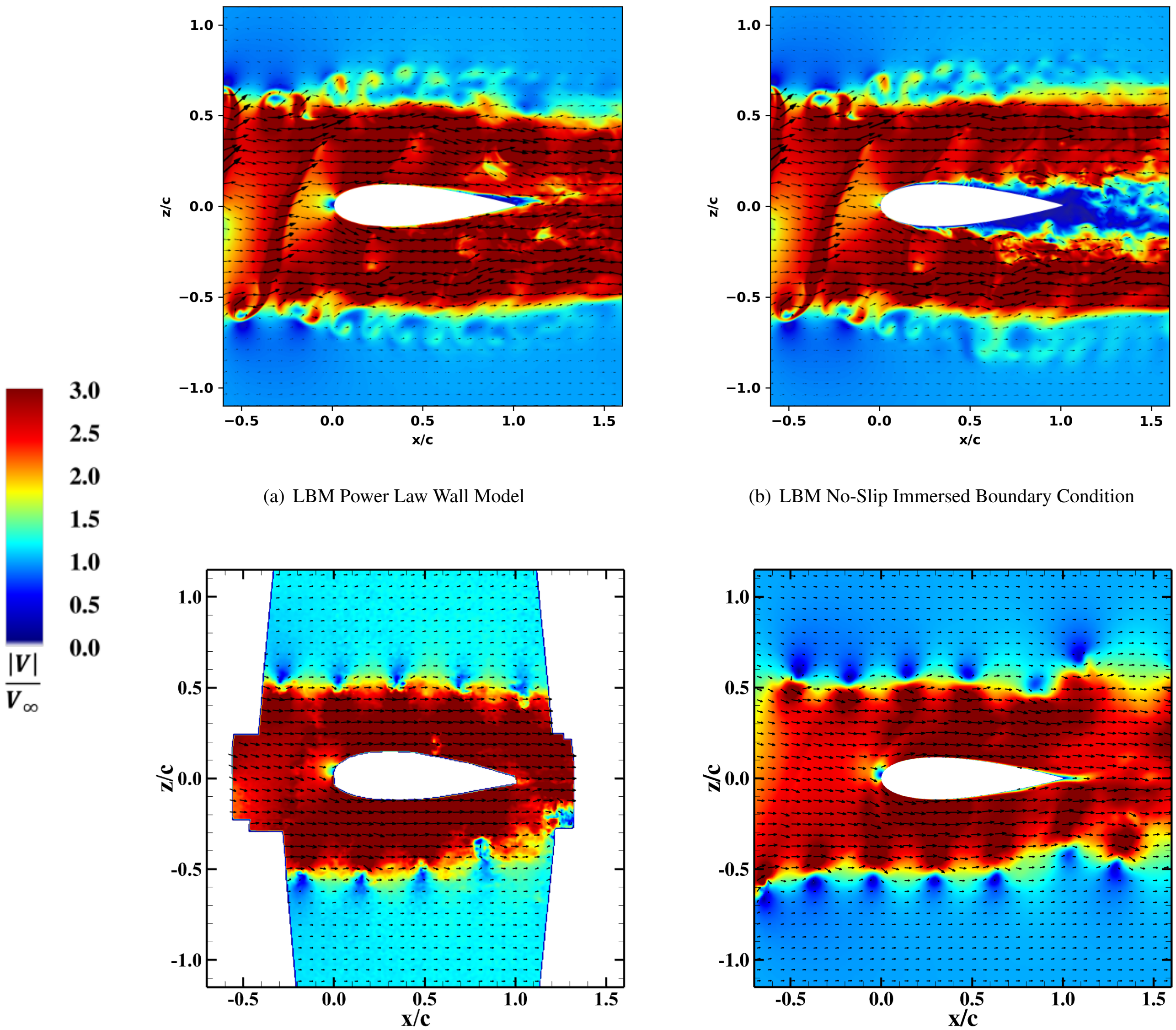

(a) LBM Power Law Wall Model

(b) LBM No-Slip Immersed Boundary Condition

(c) Wind Tunnel Measurements

(d) High-Fidelity CFD

Figure 7: Flow field comparison of the instantaneous normalized velocity magnitude to results from Ref. 21 at $y = 0.5R$ from the wing midspan for $\theta = 0°$.

A similar level of agreement was observed on the lower surface of the wing, as shown in Figure 6b. In this case, all datasets exhibited close correspondence, with improved alignment in pressure magnitude between the experimental and computational results. Notably, the pressure distributions predicted by the LBM power-law wall model and the LBM no-slip immersed boundary condition were nearly indistinguishable across both wing surfaces at this proprotor tilt angle.

This consistency aligns with the observations in Figure 7, where both of the LBM boundary condition flow fields displayed comparable behavior across the majority of the wing. The oscillations observed in the LBM pressure distributions arise from limitations in extracting data precisely at the surface and at the spanwise location of 0.5R. Due to grid alignment constraints, pressure sampling points deviate by up to ± 0.7 mm from the target plane, introducing minor variability in the recorded data.

The strong agreement among the experimental data, high-fidelity OVERFLOW CFD, and both LBM boundary conditions at $\theta = 0°$ demonstrates the capability of the LBM approach to accurately resolve surface pressures during proprotor–wing aerodynamic interactions. As this proprotor tilt angle corresponds to the forward-flight configuration, the results presented here affirm the suitability of the LBM framework for capturing complex aerodynamic interactions in fixed-wing flight conditions. Moreover, they provide a validated reference case for subsequent evaluations across a range of proprotor tilt angles.

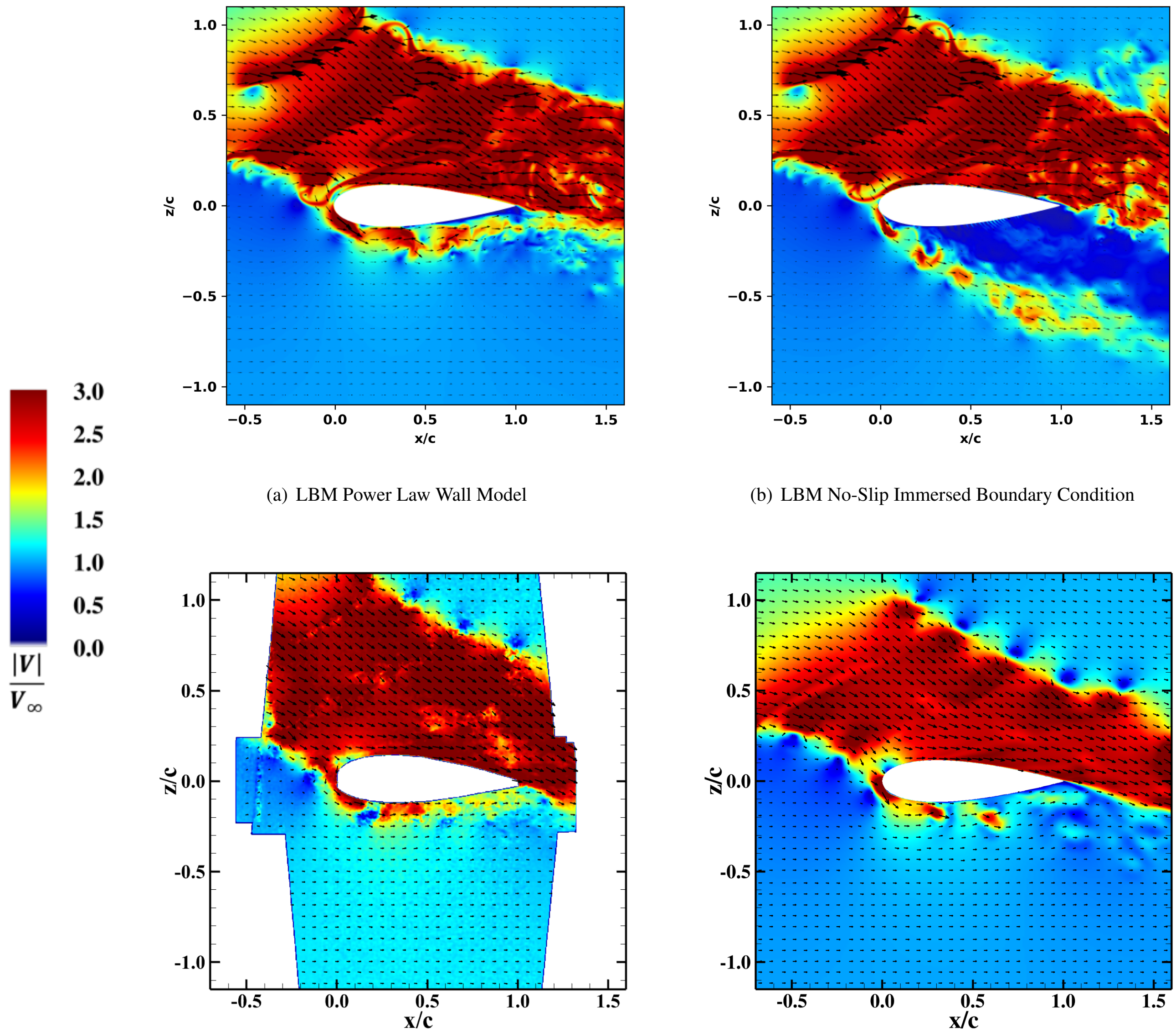

(a) LBM Power Law Wall Model

(b) LBM No-Slip Immersed Boundary Condition

(c) Wind Tunnel Measurements

(d) High-Fidelity CFD

Figure 8: Flow field comparison of the instantaneous normalized velocity magnitude to results from Ref. 21 at $y = 0.5R$ from the wing midspan for $\theta = 45°$.

The next case analyzed is shown in Figure 8 and corresponds to a proprotor tilt angle of $\theta = 45°$, a configuration representative of the midpoint in the tiltrotor transition regime. This case illustrated both the strengths and limitations of the LBM boundary conditions in resolving complex wake–wing interactions. Both the LBM power-law wall model and no-slip immersed boundary condition successfully captured the presence of high-velocity magnitude regions throughout the wake above the wing, in agreement with the experimental and high-fidelity CFD results. Furthermore, the LBM simulations exhibited comparable low-velocity patterns along the upper edge of the wake, consistent with the vortex breakdown observed in the reference data from Ref. 21. These trends suggest that the LBM is capable of modeling key features of wake breakdown and associated flow structures in this transitional regime.

Of particular interest was the region near the wing's leading edge. The experimental and high-fidelity CFD flow fields both revealed strong high-velocity flow impinging on the leading edge, followed by a sharp turn and subsequent vortex formation as the flow travels across the lower surface. The LBM power-law wall model reproduced this behavior with notable accuracy. The high-velocity flow was observed wrapping around the leading edge and decaying progressively along the lower surface, a feature consistent with the trends in both experimental and CFD visualizations.

Specifically, the light-green to yellow-red region which appeared downstream of $x/c = 0.5$ on the lower surface aligned closely with the experimental flow field, suggesting that the decay in velocity and subsequent vortex shedding are captured well. This vortex shedding also showed qualitative agreement with the high-fidelity CFD results, where the disturbed flow recombined with the wake. These observations indicate that the LBM power-law wall model is capable of resolving key aerodynamic structures, including vortex-induced flow evolution, at intermediate tilt angles.

Conversely, the LBM no-slip immersed boundary condition failed to capture several important features of the flow. While it did predict high-velocity flow across the leading edge, the flow did not wrap around onto the lower surface of the wing, deviating from the experimental and high-fidelity behavior. Instead, the flow continued along its initial trajectory, undergoing breakdown without having interacted with the wing in a physically accurate manner. This behavior resulted in the formation of an extensive low-velocity separation region along the lower surface of the wing, which was not corroborated by the experimental or high-fidelity CFD reference data. The resulting quiescent flow led to the development of a high-static-pressure zone beneath the wing that partially offset the downward momentum imparted by the proprotor wake. Consequently, the net negative lift generated by the wing was reduced. A similar effect was observed at higher proprotor tilt angles approaching $\theta = 90°$, where a prominent high-pressure separation region persisted along the lower surface, further diminishing the magnitude of the lifting force. As in previously discussed cases, this behavior reflects a limitation of the no-slip immersed boundary condition in modeling near-wall separation and wake reattachment phenomena.

Additional insight into the flow field behavior at this proprotor tilt angle is provided by the surface pressure coefficient distributions shown in Figure 9. These results indicated that the LBM power-law wall model effectively captured the overall pressure distribution trends on both the upper and lower surfaces of the wing. However, as shown in Figure 9b, it overpredicted the magnitude of the pressure peak on the lower surface when compared to the high-fidelity CFD results. In contrast, the pressure distribution over the upper surface aligned closely with the high-fidelity CFD data, demonstrating the capability of the LBM power-law wall model to resolve complex surface pressure variations induced by proprotor–wake interactions.

The LBM no-slip immersed boundary condition, on the other hand, significantly underpredicted the pressure over the lower surface of the wing, as illustrated in Figure 9b. This underprediction is consistent with the low-velocity region observed across the lower surface in the corresponding flow field visualization shown in Figure 8. That region was associated with elevated static pressure, which correspondingly reduced the magnitude of the local pressure coefficient. Interestingly, the pressure values predicted by the no-slip immersed boundary condition exhibited good agreement with the experimental measurements on the lower surface. On the upper surface, the no-slip immersed boundary condition exhibited good agreement with both the experimental and LBM power-law results, though some oscillations were present as previously noted.

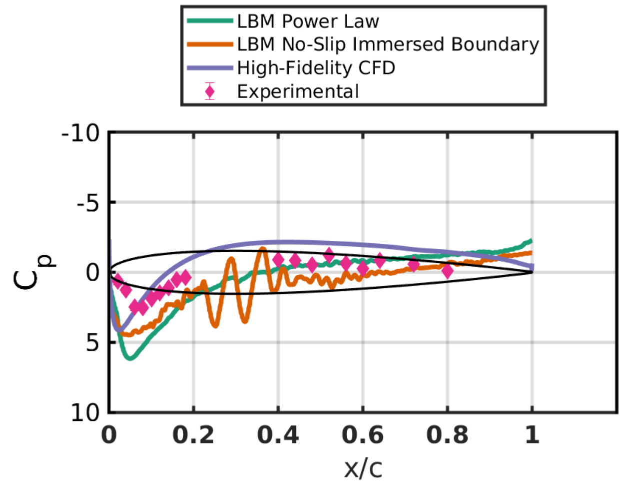

a) Wing Upper Surface

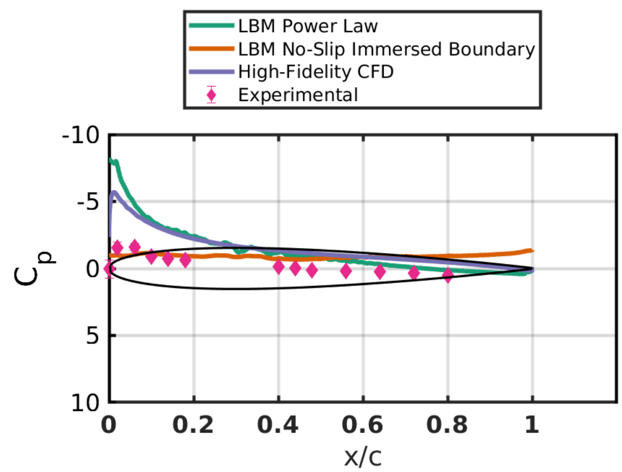

b) Wing Lower Surface

Figure 9: Pressure coefficient comparison to results from Ref. 21 at $y = -0.5R$ from the wing midspan for $\theta = 45°$.

Collectively, the pressure coefficient distributions shown in Figure 9 underscore the capability of the LBM framework to accurately and efficiently capture surface pressure fields on aerodynamic configurations undergoing complex proprotor–wake interactions characteristic of the tiltrotor transition regime.

The final set of flow field comparisons corresponds to a proprotor tilt angle of $\theta = 90°$, representative of the hover condition in a tiltrotor configuration. The corresponding results are depicted in Figure 10. As with the previously analyzed proprotor angles, the LBM simulations demonstrated a strong capability to resolve the primary features of the wake. In particular, both LBM boundary condition implementations captured the bulk structure of the proprotor wake with high fidelity, as strong high-velocity cores and vortex breakdown appeared along the wake periphery, especially along the right edge. Those features were consistent with experimental observations and the high-fidelity CFD results presented in Ref. 21.

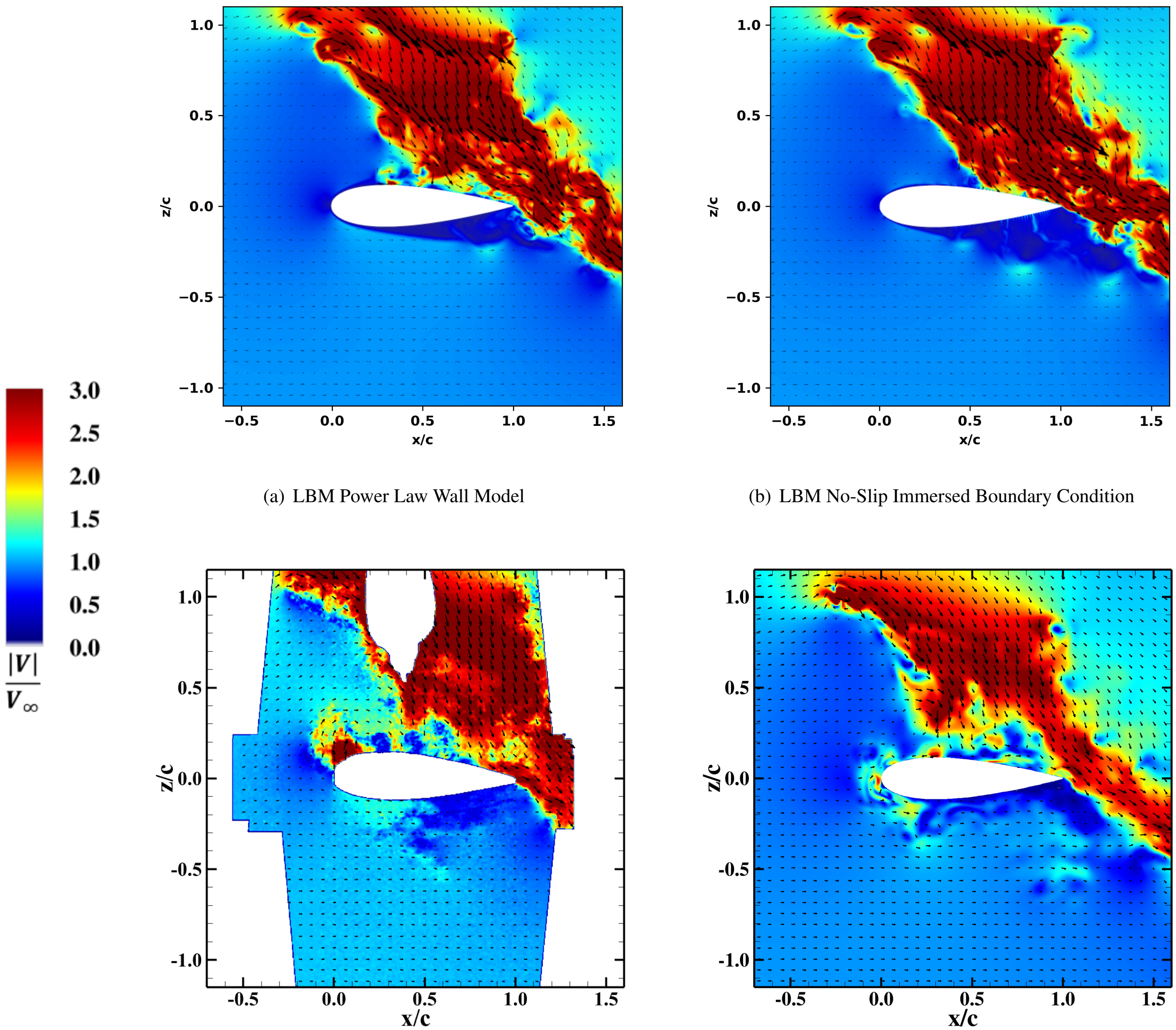

(a) LBM Power Law Wall Model

(b) LBM No-Slip Immersed Boundary Condition

(c) Wind Tunnel Measurements

(d) High-Fidelity CFD

Figure 10: Flow field comparison of the instantaneous normalized velocity magnitude to results from Ref. 21 at $y = 0.5R$ from the wing midspan for $\theta = 90°$.

Despite these strengths, several discrepancies were again evident. The experimental flow visualization showed a broad region of high-velocity magnitude flow near the leading edge of the upper wing surface. While the high-fidelity CFD did not replicate this feature identically, it did capture significant flow which wrapped around the leading edge and transitioned onto the lower surface, where it developed into a highly unsteady, vortex-laden flow that eventually broke down near the trailing edge within a well-defined separation zone. This complex flow behavior was not reproduced by either LBM boundary formulation, both of which failed to capture any appreciable upstream-directed flow impinging on the leading edge.

However, both LBM models did predict a sizable separation region on the lower surface of the wing. The nature of this separation differed between the two models: the power-law wall model resulted in a relatively smooth, laminar separation region, while the no-slip immersed boundary condition more accurately captured the turbulent breakdown and vortex shedding behavior, consistent with high-Reynolds-number separation phenomena. This again suggests that the no-slip immersed boundary formulation is better suited for modeling complex separated flows on the suction side of lifting surfaces. The separation regions observed in both LBM simulations exhibited effects analogous to those in the $\theta = 45°$ case, wherein elevated static pressure over the lower surface led to a reduction in lifting force magnitude.

Further discrepancies were observed on the upper surface of the wing. Both the experimental and high-fidelity CFD datasets indicated the presence of a low-velocity magnitude region which extended over the upper surface—approximately from $x/c = 0.3$ to $x/c = 0.7$ in the experimental case, and from $x/c = 0.4$ to $x/c = 0.9$ in the CFD solution. The LBM power-law wall model captured this feature to a limited extent, as it exhibited a localized low-velocity region centered near $x/c = 0.35$. However, this feature dissipated rapidly downstream, where it transitioned into a region of increased velocity and turbulent activity, which is not fully consistent with the reference datasets. In contrast, the LBM no-slip immersed boundary formulation did not reproduce any appreciable low-velocity region over the upper surface, indicating a shortcoming in its ability to capture suction-side boundary layer development and pressure recovery under these conditions.

Additional insights into the accuracy of the LBM boundary conditions for the $\theta = 90°$ case can be obtained by analyzing the pressure coefficient distributions shown in Figure 11. Along the lower surface of the wing, both LBM boundary treatments showed strong consistency with the high-fidelity CFD and experimental results over the entire wing.

Some differences were observed on the upper surface of the wing, where the divergence between the LBM, CFD, and wind tunnel pressures was more pronounced. In the forward portion of the wing, specifically over the second fifth of the chord, the high-fidelity CFD results exhibited a negative pressure coefficient, indicative of a low-velocity flow region over the wing upper surface. A similar pressure drop appeared in the experimental data at approximately the same location on the wing, although neither LBM boundary condition replicated the trend. This is consistent with the presence of a low-velocity flow region above the wing in both the high-fidelity CFD and experimental flow fields in Figure 10, which was absent in the LBM predictions. The inability to accurately replicate this suction peak underscores a key limitation of the current LBM formulations, particularly under high-incidence flow conditions where leading-edge effects strongly influence surface pressure distribution.

Another difference appeared near the trailing edge of the wing upper surface, as shown in Fig. 11a. Both of the LBM boundary conditions exhibited a small pressure peak at approximately $x/c = 0.9$, whereas the high-fidelity CFD data predicted a slightly negative pressure coefficient at the same location. This discrepancy was likely caused by some minor vortex wrapping around the trailing edge of the wing in the LBM simulations. Aside from this localized deviation, both of the LBM boundary conditions accurately predicted the surface pressure distribution over the wing in the hover configuration.

Wing and Proprotor Loads

The initial test case considered in this study involved an isolated wing operating under free-air conditions. All simulation parameters are given in the previous Table 1. The simulation protocol utilized in this work mirrors the methodology employed by Sridhar et al. (Ref. 21) in their experiments and OVERFLOW CFD analyses. Aerodynamic forces acting on the wing were calculated through momentum exchange within the LBM framework. These forces were subsequently used to compute the corresponding lift and drag coefficients, the results of which are summarized in Table 2.

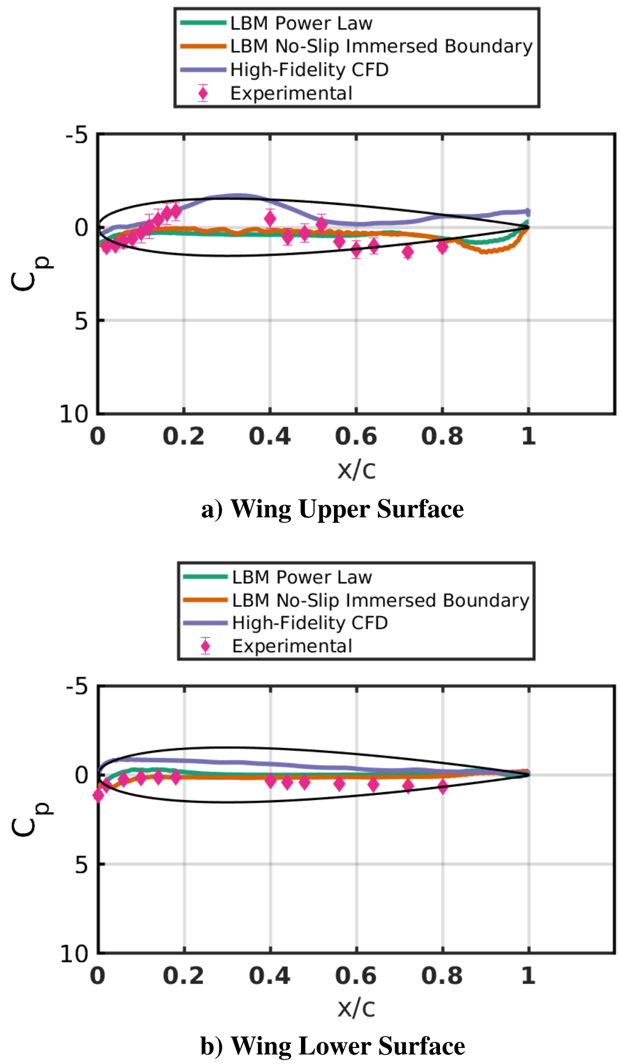

Figure 11: Pressure coefficient comparison to results from Ref. 21 at $y = -0.5R$ from the wing midspan for $\theta = 90°$.

Table 2: Time-averaged wing load coefficients for isolated wing case

Method	C_D	C_L
High-Fidelity Computational	0.0212 ± 0.000210	0.000991 ± 0.00123
LBM Power Law Wall Model	0.0418 ± 0.00013	-0.0323 ± 0.0079
LBM No-Slip Immersed Boundary	0.1211 ± 0.00048	-0.0416 ± 0.0046
Experimental	0.0425 ± 0.0044	0.0075 ± 0.0074

As shown in Table 2, the drag coefficient predicted using the LBM power-law wall model exhibits strong agreement with both experimental and high-fidelity OVERFLOW CFD results. Notably, the power-law prediction lies between the values reported by Sridhar et al. (Ref. 21), with closer proximity to the experimentally measured drag coefficient than the high-fidelity CFD counterpart. Moreover, the predicted drag falls within the unsteadiness bounds of the experimental data, underscoring the capability of the explicit power-law wall model to accurately capture viscous drag over solid surfaces.

In contrast, the drag coefficient computed using the LBM no-slip immersed boundary condition was significantly overpredicted, with a value approximately 300% higher than the experimental reference. This overestimation was likely attributed to the limited resolution over the surface of the wing. As previously discussed, the implemented resolution in this work gives a value of $y^+ \approx 25$ near the wing, contrary to the established standard of $y^+ = 1$. This resolution is suitable for explicit boundary layer modeling conditions, such as the explicit power-law, however the no-slip immersed boundary condition is not one of these. The relatively low resolution for the no-slip immersed boundary condition caused the boundary layer thickness to be severely overpredicted. This led to a notable increase in pressure drag over the wing and an elevated total drag coefficient, as evidenced by the prominent separation region shown in Figure 7. This discrepancy highlights the sensitivity of drag prediction to the chosen near-wall modeling approach within LBM frameworks.

The lift coefficient predictions, however, were found to deviate from theoretical expectations. For a symmetric airfoil at zero angle of attack subjected to steady inflow—conditions matching those of the present simulation, the lift coefficient should nominally be zero. Both LBM boundary conditions studied herein, however, predicted a non-negligible negative lift. This underprediction of lifting force suggests a systematic shortcoming in the boundary modeling that adversely affects pressure distribution over the airfoil surface. Potential causes for this discrepancy will be further examined in subsequent sections.

The computed drag and lift coefficients for each proprotor tilt angle simulated are presented in Figures 12 and 13, alongside the comparative data from Sridhar et al. (Ref. 21). Tabulated values are provided in Table 3. The trends observed are generally consistent with those identified in the isolated wing case. As shown in Figure 12, the no-slip immersed immersed boundary condition (denoted in orange) systematically overpredicted drag across all simulated tilt angles. In several cases, the predicted drag exceeded the experimentally measured values by more than a factor of two. This persistent overestimation highlights a fundamental limitation of the no-slip immersed boundary formulation: its inability to accurately capture surface shear and pressure effects, which are critical for reliable drag prediction.

In contrast, the explicit power-law wall model (shown in red) demonstrated substantially improved agreement with both the experimental data and high-fidelity OVERFLOW CFD simulations. For the initial five tilt angles evaluated, the power-law results closely aligned with the high-fidelity CFD values, frequently falling within the reported unsteadiness bounds. At higher tilt angles, a deviation from the high-fidelity trend was observed. Specifically, the LBM power-law solution exhibited an increase in drag between 45° and 60°, whereas both the experimental data and high-fidelity CFD results indicated a marked decrease over the same range. This divergence may point to an underlying limitation of the power-law wall model in capturing complex flow features associated with high tilt-angle configurations, leaving room for further development.

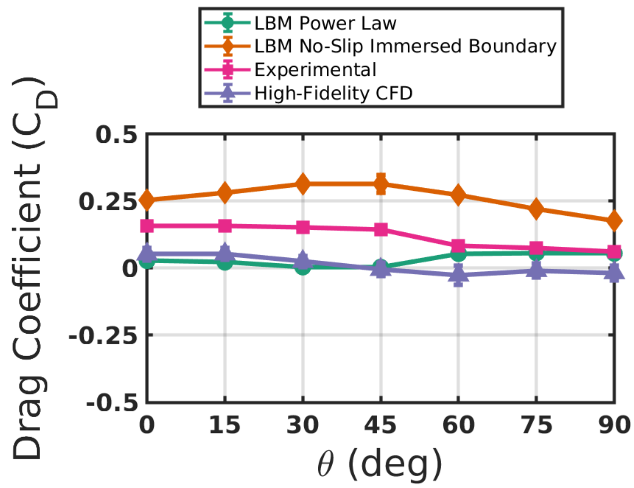

Figure 12: Drag coefficient comparison to results from Ref. 21 for all proprotor tilt angles

Although the overall level of agreement lends credibility to the power-law model, the unexpected drag behavior at higher tilt angles warrants further investigation. It may provide critical insight into the boundary condition's accuracy limits and the aerodynamic mechanisms driving divergence between LBM and high-fidelity OVERFLOW CFD results.

Figure 13 presents the computed lift coefficients for both LBM boundary conditions across the full range of simulated proprotor tilt angles, alongside the experimental and high-fidelity OVERFLOW CFD results reported by Sridhar et al. (Ref. 21). At $\theta = 0°$, the high-fidelity OVERFLOW CFD solution predicted a lift coefficient near zero, as expected for a symmetric airfoil at zero angle of attack under steady inflow. The experimental results, however, report a significantly non-zero lift, suggesting the presence of measurement asymmetries or subtle flow disturbances. Both LBM boundary conditions predicted negative lift coefficients at this tilt angle, consistent with the behavior observed in the isolated wing simulations discussed previously.

As the tilt angle increased to $\theta = 15°$, both LBM boundary models showed improved agreement with the experimental and CFD data. While the LBM simulations slightly underpredicted lift relative to the results from Sridhar et al. (Ref. 21), the overall trend and magnitude remain comparable, suggesting adequate performance of both the power-law wall model and the no-slip immersed wall treatment in moderate tilt regimes.

For θ values up to 45°, the no-slip immersed boundary condition maintained qualitative agreement with the experimental and high-fidelity CFD results, capturing the expected decrease in lift as the rotor wake increasingly impinges on the upper

Table 3: Time-averaged wing load coefficients

Method	θ (°)	C_D	C_L
High-Fidelity Computational	0	0.0521 ± 0.0234	0.0036 ± 0.0330
LBM Power Law Wall Model		0.0275 ± 0.0092	-0.0564 ± 0.0116
LBM No-Slip Immersed Boundary		0.2521 ± 0.0062	-0.0397 ± 0.0135
Experimental		0.1579 ± 0.0088	0.1509 ± 0.0052
High-Fidelity Computational	15	0.0524 ± 0.0225	-0.1161 ± 0.0342
LBM Power Law Wall Model		0.0218 ± 0.0119	-0.0681 ± 0.0302
LBM No-Slip Immersed Boundary		0.2802 ± 0.0112	-0.0666 ± 0.0328
Experimental		0.1578 ± 0.0060	-0.0937 ± 0.0083
High-Fidelity Computational	30	0.0243 ± 0.0199	-0.2176 ± 0.0486
LBM Power Law Wall Model		0.0037 ± 0.0119	-0.0826 ± 0.0269
LBM No-Slip Immersed Boundary		0.3132 ± 0.0086	-0.1338 ± 0.0200
Experimental		0.1515 ± 0.0114	-0.2467 ± 0.0116
High-Fidelity Computational	45	-0.0051 ± 0.0243	-0.2575 ± 0.0545
LBM Power Law Wall Model		0.0037 ± 0.0163	-0.0322 ± 0.0347
LBM No-Slip Immersed Boundary		0.3139 ± 0.0323	-0.1899 ± 0.0186
Experimental		0.1424 ± 0.0090	-0.2401 ± 0.0114
High-Fidelity Computational	60	-0.0263 ± 0.0355	-0.2464 ± 0.0523
LBM Power Law Wall Model		0.0538 ± 0.0051	0.0120 ± 0.0347
LBM No-Slip Immersed Boundary		0.2718 ± 0.0096	-0.1415 ± 0.0079
Experimental		0.0842 ± 0.0064	-0.2452 ± 0.0147
High-Fidelity Computational	75	-0.0093 ± 0.0258	-0.2581 ± 0.0492
LBM Power Law Wall Model		0.0565 ± 0.0030	-0.0251 ± 0.0441
LBM No-Slip Immersed Boundary		0.2200 ± 0.0085	-0.1018 ± 0.0082
Experimental		0.0764 ± 0.0071	-0.2547 ± 0.0097
High-Fidelity Computational	90	-0.0175 ± 0.0276	-0.3046 ± 0.0765
LBM Power Law Wall Model		0.0549 ± 0.0068	-0.0081 ± 0.0589
LBM No-Slip Immersed Boundary		0.1767 ± 0.0085	-0.0832 ± 0.0143
Experimental		0.0599 ± 0.0098	-0.1911 ± 0.0164

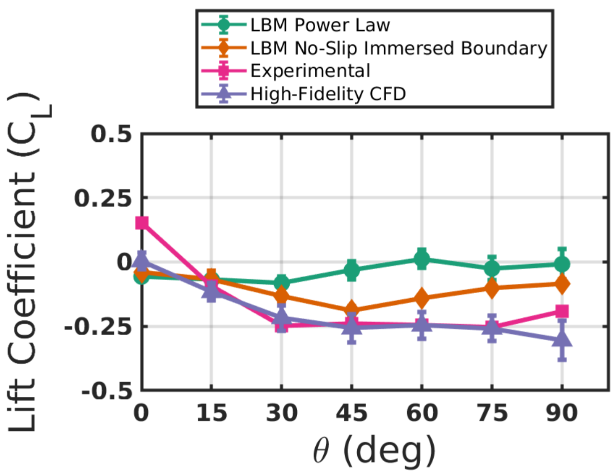

Figure 13: Lift coefficient comparison to results from Ref. 21 for all proprotor tilt angles

surface of the wing. In contrast, the power-law wall model exhibited an anomalous trend: after decreasing, the lift coefficient begins to increase significantly, diverging from both reference datasets. This discrepancy becomes more pronounced at higher tilt angles.

As θ increased to 90°, the power-law model predicted a substantial increase in lift, ultimately producing a lift coefficient close to zero for the final three tilt angles. This outcome directly contradicts both the experimental and CFD results, which showed continued reduction in lift due to increased wake-induced flow disruption on the upper surface. The no-slip immersed wall treatment also deviated from reference trends beyond $\theta = 45°$, though it maintained negative lift coefficients throughout the tilt sweep. This divergence stems from the separation region visible on the lower surface in Figures 8 and 10, where low-velocity, high static-pressure flow opposes the downforce induced by the proprotor wake.

The discrepancies, particularly the unphysical lift predictions from the power-law model at higher tilt angles, highlight limitations in the wall model's ability to capture flow reversal, separation, and unsteady wake interactions. While previously presented flow field and pressure data suggested strong agreement with reference solutions, these were extracted in two-dimensional planes. In contrast, the lift and drag coefficients reflect integrated three-dimensional effects, indicating that flow outside the proprotor wake may not be resolved with sufficient accuracy. This represents a key area for future refinement.

Figures 14 and 15, along with Table 4, present the computed thrust and torque coefficients for the proprotor across all simulated flight conditions. Results from both LBM boundary condition models are shown alongside the experimental and high-fidelity blade-resolved OVERFLOW CFD data reported by Sridhar et al. (Ref. 21). In the LBM framework, the actuator line representation of the proprotor was trimmed to match the experimentally measured thrust. As such, a strong correlation between the LBM and experimental thrust coefficient results is expected.

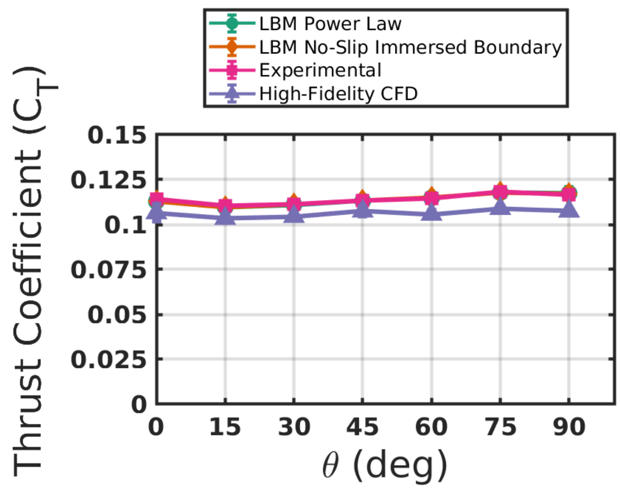

Figure 14: Thrust coefficient comparison to results from Ref. 21 for all proprotor tilt angles

This correlation is indeed observed, as illustrated in Figure 14. Both the no-slip immersed boundary condition (orange) and the explicit power-law wall model (green) exhibited close agreement with the experimental thrust coefficients across nearly all simulated proprotor tilt angles. The largest deviation occurred at $\theta = 30°$, where the LBM results slightly overpredicted the thrust coefficient. Nevertheless, the LBM-predicted values remained within the experimental unsteadiness bounds, reinforcing the model's reliability in this regime.

The high-fidelity OVERFLOW CFD results produced thrust coefficients that are generally lower in magnitude and exhibit a vertical offset relative to both the LBM and experimental data. However, they followed a consistent trend, indicating

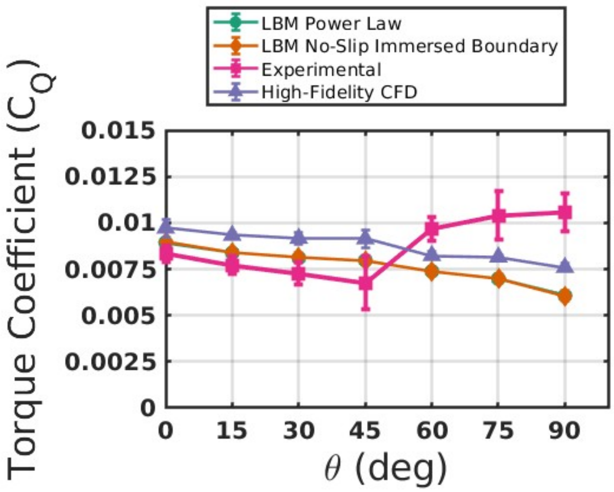

Figure 15: Torque coefficient comparison to results from Ref. 21 for all proprotor tilt angles

Table 4: Time-averaged proprotor load coefficients

Method	θ (°)	C_T	C_Q
High-Fidelity Computational	0	0.1065 ± 0.0046	0.0097 ± 0.0004
LBM Power Law Wall Model		0.1129 ± 0.0008	0.0089 ± 0.00005
LBM No-Slip Immersed Boundary		0.1131 ± 0.0007	0.0090 ± 0.00004
Experimental		0.1141 ± 0.0004	0.0083 ± 0.0004
High-Fidelity Computational	15	0.1034 ± 0.0023	0.0093 ± 0.0001
LBM Power Law Wall Model		0.1096 ± 0.0007	0.0084 ± 0.00004
LBM No-Slip Immersed Boundary		0.1098 ± 0.00005	0.0084 ± 0.00003
Experimental		0.1105 ± 0.0022	0.0077 ± 0.0005
High-Fidelity Computational	30	0.1045 ± 0.0017	0.0092 ± 0.0003
LBM Power Law Wall Model		0.1110 ± 0.0021	0.0081 ± 0.0003
LBM No-Slip Immersed Boundary		0.1113 ± 0.0022	0.0081 ± 0.0003
Experimental		0.1111 ± 0.0014	0.0073 ± 0.0006
High-Fidelity Computational	45	0.1074 ± 0.0026	0.0091 ± 0.0005
LBM Power Law Wall Model		0.1131 ± 0.0012	0.0080 ± 0.0001
LBM No-Slip Immersed Boundary		0.1133 ± 0.0010	0.0080 ± 0.0001
Experimental		0.1133 ± 0.0013	0.0068 ± 0.0014
High-Fidelity Computational	60	0.1057 ± 0.0021	0.0082 ± 0.0002
LBM Power Law Wall Model		0.1148 ± 0.0018	0.0074 ± 0.0002
LBM No-Slip Immersed Boundary		0.1148 ± 0.0019	0.0074 ± 0.0002
Experimental		0.1144 ± 0.0020	0.0097 ± 0.0006
High-Fidelity Computational	75	0.1089 ± 0.0016	0.0082 ± 0.0001
LBM Power Law Wall Model		0.1178 ± 0.0021	0.0070 ± 0.0002
LBM No-Slip Immersed Boundary		0.1179 ± 0.0022	0.0070 ± 0.0002
Experimental		0.1182 ± 0.0012	0.0104 ± 0.0013
High-Fidelity Computational	90	0.1074 ± 0.0016	0.0076 ± 0.0002
LBM Power Law Wall Model		0.1174 ± 0.0032	0.0061 ± 0.0003
LBM No-Slip Immersed Boundary		0.1171 ± 0.0026	0.0061 ± 0.0003
Experimental		0.1165 ± 0.0008	0.0106 ± 0.0010

that the overall thrust behavior is captured across all modeling approaches. These findings support the conclusion that the actuator line method, when implemented within the LBM framework, is capable of accurately and efficiently predicting thrust generation by a proprotor under a range of operating conditions.

An informative trend is observed in the torque coefficient data presented in Figure 15. For the first four proprotor tilt angles, the torque coefficients predicted by both LBM boundary conditions consistently fell between the wind tunnel measurements and the high-fidelity CFD results, effectively bisecting the two. This alignment suggests that the LBM implementation captured the primary aerodynamic loading characteristics of the proprotor with reasonable accuracy in this lower tilt regime.

As the tilt angle increased beyond $\theta = 45°$, the experimental torque coefficients exhibited a marked increase, accompanied by a noticeable rise in unsteadiness. This rapid escalation in torque, unaccounted for by either the LBM or high-fidelity OVERFLOW CFD simulations, suggests the presence of experimental flow phenomena not captured by current computational models. Such differences may be indicative of complex rotor–wake interactions, flow separation, or structural coupling effects, and represent an important avenue for future model refinement and investigation.

Despite this divergence from wind tunnel measurements at higher tilt angles, the LBM and high-fidelity CFD torque predictions followed a nearly identical trend, differing primarily in magnitude rather than behavior. This consistency in trend between an actuator line representation within LBM and body-fitted grids in a conventional CFD framework highlights the capability of the actuator line method to reliably predict proprotor aerodynamic loads.

The LBM simulations accurately predicted the majority of the complex aerodynamic interactions characteristic of the tiltrotor transition regime, while offering a substantial improvement in computational efficiency compared to the high-fidelity OVERFLOW CFD of Sridhar et al. (Ref. 21). Specifically, the LBM approach simulated 70 proprotor revolutions in only 100 minutes using eight NVIDIA A100 GPUs, whereas the high-fidelity CFD required 21 hours to complete a single proprotor revolution on 768 CPU nodes. Thus, the LBM framework with actuator-line rotor model delivered mid-fidelity accuracy while achieving speedups of several orders of magnitude over high-fidelity blade-resolved OVERFLOW CFD, demonstrating its effectiveness as a tool for rapid, yet accurate, aerodynamic analysis of proprotor–wing interactions.

SUMMARY AND CONCLUSIONS

This study evaluated the capability of a mid-fidelity Lattice-Boltzmann Method (LBM) model to simulate the complex aerodynamic interactions between a proprotor and a fixed wing across a wide range of proprotor tilt angles occurring during the conversion (or transition) maneuver. Two wing wall boundary treatments, the explicit power-law wall model and the no-slip immersed boundary condition, were implemented to assess near-wall behavior, while an actuator line approach was developed and employed to efficiently represent the tilting proprotor. To assess physical accuracy, the LBM simulations were compared against high-fidelity CFD and wind tunnel measurements of proprotor and wing loads, surface pressures, and flow fields.

The following specific conclusions have been drawn:

1. Flow field comparisons to experiment and high-fidelity CFD confirmed accurate resolution of proprotor wake structures for both LBM boundary conditions, including vortex breakdown and high-rotational velocity vortex cores. The no-slip immersed boundary treatment better

predicted large-scale flow separation zones, but overestimated their extent and associated drag. The explicit power-law wall model more accurately captured nuanced flow features, such as leading-edge acceleration and vortex development, especially at intermediate tilt angles (e.g., $\theta = 45°$)

2. The LBM explicit power-law wall model predicted drag forces on the wing with high accuracy across all proprotor tilt angles, shown by strong agreement with experimental and high-fidelity CFD results. In contrast, the LBM no-slip immersed boundary wall treatment consistently overpredicted drag due to the relatively coarse grid resolution at the wing surface, which caused an overprediction of the boundary layer thickness and flow separation, and in turn increased pressure drag over the wing.

3. The LBM power-law wall model underpredicted lift beyond a proprotor tilt angle of $\theta = 15°$, likely due to its assumption of zero wall-normal velocity at a reference point, which causes inaccurate pressure recovery. The LBM no-slip immersed boundary condition more reliably captured lift trends at tilt angles up to $\theta = 45°$, but also deteriorated at high incidence, limiting lift generation due to an incorrectly resolved separation region on the lower surface of the wing.

4. The actuator line model implementation within the LBM framework showed excellent agreement with experimental proprotor thrust coefficients when trimmed to test conditions. Torque coefficient trends and magnitudes correlated well with high-fidelity CFD, indicating the method's ability to replicate key rotor-induced effects without using body-fitted grids.

5. The LBM simulations captured the majority of the proprotor–wing interactions with good accuracy while offering substantial computational efficiency. One proprotor revolution was simulated in approximately 1.4 minutes with the LBM, compared to 21 hours per revolution for the high-fidelity blade-resolved OVERFLOW CFD. This corresponds to a computational speedup of several orders of magnitude, highlighting the efficiency of the LBM framework relative to high-fidelity Navier–Stokes methods while not sacrificing much physical accuracy in the results.

6. At low proprotor tilt angles, the explicit power-law wall model captured overall wing surface pressure trends but exaggerated gradients due to wall-normal velocity assumptions. The no-slip immersed boundary condition more accurately predicted suction-side pressures but misrepresented the lower surface due to overpredicted separation zones. At high proprotor tilt angles, both models identified the pressure peaks but misplaced their locations; the power-law wall model correlated better with peak magnitudes, while the no-slip immersed boundary condition underpredicted them.

The present work demonstrated the feasibility of simulating complex proprotor–wing aerodynamic interactions by LBM simulations. Further refinement, particularly in wall-normal velocity treatment and resolution dependence, is essential for improving physical accuracy across the range of proprotor tilt angles which occur during the tiltrotor conversion maneuver.

ACKNOWLEDGMENTS

This work was funded by the US Navy under STTR contract number N68335-21-C-0336, with Susan Polsky serving as the technical monitor. Any opinion, findings, and conclusions or recommendations expressed in this material are those of the authors and do not necessarily reflect the views of the United States Government.

The authors would like to thank Shreyas Srivathsan and Pranav Sridhar for their assistance in providing the experimental and high-fidelity CFD validation data.

Author Contact Information

Alex Natelson - anatelson3@gatech.edu

Duncan Waanders - dwaanders3@gatech.edu

Shreyas Ashok - sashok@gatech.edu

Juergen Rauleder - juergen.rauleder@gatech.edu

REFERENCES

1. Sugawara, H., and Tanabe, Y., "Numerical Investigation of Rotor/Wing Aerodynamic Interactions at High Advance Ratios," *Journal of Aircraft*, Vol. 56, (6), 2019, pp. 2285–2298. DOI: 10.2514/1.C035370.

2. Renaud, T., O'Brien, D., Smith, M., and Potsdam, M., "Evaluation of Isolated Fuselage and Rotor-Fuselage Interaction Using CFD," *Annual Forum Proceedings - American Helicopter Society*, Vol. 1, 02 2004. DOI: 10.4050/JAHS.53.3.

3. Costes, M., Renaud, T., and and, B. R., "Rotorcraft simulations: a challenge for CFD," *International Journal of Computational Fluid Dynamics*, Vol. 26, (6-8), 2012, pp. 383–405. DOI: 10.1080/10618562.2012.726710.

4. Wilcox, D. C., *et al.*, *Turbulence modeling for CFD*, Vol. 2, DCW industries La Canada, CA, 1998.

5. Zhai, Z. J., Zhang, Z., Zhang, W., and Chen, Q. Y., "Evaluation of Various Turbulence Models in Predicting Airflow and Turbulence in Enclosed Environments by CFD: Part 1—Summary of Prevalent Turbulence Models," *HVAC&R Research*, Vol. 13, (6), 2007, pp. 853–870. DOI: 10.1080/10789669.2007.10391459.

6. Zhang, Z., Zhang, W., Zhai, Z. J., and Chen, Q. Y., "Evaluation of Various Turbulence Models in Predicting Airflow and Turbulence in Enclosed Environments by CFD: Part 2—Comparison with Experimental Data from Literature," *HVAC&R Research*, Vol. 13, (6), 2007, pp. 871–886. DOI: 10.1080/10789669.2007.10391460.

7. Aubin, J., Fletcher, D., and Xuereb, C., "Modeling turbulent flow in stirred tanks with CFD: the influence of the modeling approach, turbulence model and numerical scheme," *Experimental Thermal and Fluid Science*, Vol. 28, (5), 5th international conference on Gas-Liquid and Gas-Liquid-Solid Reactor Engineering, 2004, pp. 431–445. DOI: 10.1016/j.expthermflusci.2003.04.001.

8. Thompson, J. F., "Grid generation techniques in computational fluid dynamics," *AIAA Journal*, Vol. 22, (11), 1984, pp. 1505–1523. DOI: 10.2514/3.8812.

9. Hernandez-Perez, V., Abdulkadir, M., and Azzopardi, B., "Grid Generation Issues in the CFD Modelling of Two-Phase Flow in a Pipe," *The Journal of Computational Multiphase Flows*, Vol. 3, (1), 2011, pp. 13–26. DOI: 10.1260/1757-482X.3.1.13.

10. Samareh, J. A., "Status and Future of Geometry Modeling and Grid Generation for Design and Optimization," *Journal of Aircraft*, Vol. 36, (1), 1999, pp. 97–104. DOI: 10.2514/2.2417.

11. Kulshreshtha, A., Gupta, S. K., and Singhal, P., "FEM/CFD analysis of wings at different angle of attack," *Materials Today: Proceedings*, Vol. 26, 10th International Conference of Materials Processing and Characterization, 2020, pp. 1638–1643. DOI: 10.1016/j.matpr.2020.02.342.

12. Suresh, C., Ramesh, K., and Paramaguru, V., "Aerodynamic performance analysis of a non-planar C-wing using CFD," *Aerospace Science and Technology*, Vol. 40, 2015, pp. 56–61. DOI: 10.1016/j.ast.2014.10.014.

13. Prisacariu, V., "CFD Analysis of UAV Flying Wing," *INCAS BULLETIN*, Vol. 8, 09 2016, pp. 65–72. DOI: 10.13111/2066-8201.2016.8.3.6.

14. Kasmaiee, S., Kasmaiee, S., and Farshad, A., "Unsteady CFD simulation of a rotor blade under various wind conditions," *Scientific Reports*, Vol. 14, (1), Aug 2024, pp. 19176. DOI: 10.1038/s41598-024-70350-5.

15. Song, Y., and Perot, J. B., "CFD Simulation of the NREL Phase VI Rotor," *Wind Engineering*, Vol. 39, (3), 2015, pp. 299–309. DOI: 10.1260/0309-524X.39.3.299.

16. Yeo, H., Potsdam, M., Ortun, B., and Truong, K. V., "High-Fidelity Structural Loads Analysis of the ONERA 7A Rotor," *Journal of Aircraft*, Vol. 54, (5), 2017, pp. 1825–1839. DOI: 10.2514/1.C034286.

17. Bechmann, A., Sørensen, N. N., and Zahle, F., "CFD simulations of the MEXICO rotor," *Wind Energy*, Vol. 14, (5), 2011, pp. 677–689. DOI: 10.1002/we.450.

18. Cao, J., Zhu, W., Shen, W., Sørensen, J. N., and Wang, T., "Development of a CFD-Based Wind Turbine Rotor Optimization Tool in Considering Wake Effects," *Applied Sciences*, Vol. 8, (7), 2018. DOI: 10.3390/app8071056.

19. Felker, F. F., and Light, J. S., "Aerodynamic Interactions Between a Rotor and Wing in Hover," *Journal of the American Helicopter Society*, Vol. 33, (2), 1988, pp. 53–61. DOI: doi:10.4050/JAHS.33.53.

20. Chen, W.-H., and Rauleder, J., "Unsteady Loads of a Scaled Rotor on and Near the Landing Deck of the NATO Generic Destroyer with Concurrent Stereo PIV and Surface Pressure Measurements," *Journal of the American Helicopter Society*, Vol. 69, 10 2024. DOI: 10.4050/JAHS.69.042008.

21. Sridhar, P., Srivathsan, S., Rauleder, J., and Smith, M., "Physics of the Interactional Proprotor–Wing Aerodynamics During the Tiltrotor Conversion Maneuver," Vertical Flight Society's 81st Annual Forum & Technology Display, Virginia Beach, VA, 05 2025. DOI: 10.4050/F-0081-2025-271.

22. Krüger, T., Kusumaatmaja, H., Kuzmin, A., Shardt, O., Silva, G., and Viggen, E. M., *The Lattice Boltzmann Method*, Graduate Texts in Physics, Springer, first edition, 2017. DOI: 10.1007/978-3-319-44649-3.

23. Körner, C., Pohl, T., Rüde, U., Thürey, N., and Zeiser, T., *Parallel Lattice Boltzmann Methods for CFD Applications*, Springer Berlin Heidelberg, Berlin, Heidelberg, 2006, pp. 439–466.

24. Kuznik, F., Obrecht, C., Rusaouen, G., and Roux, J.-J., "LBM based flow simulation using GPU computing processor," *Computers Mathematics with Applications*, Vol. 59, (7), Mesoscopic Methods in Engineering and Science, 2010, pp. 2380–2392. DOI: 10.1016/j.camwa.2009.08.052.

25. Wang, Y., Decker, J., and Pardyjak, E. R., "Large-Eddy Simulations of Turbulent Flows around Buildings Using the Atmospheric Boundary Layer Environment–Lattice Boltzmann Model (ABLE-LBM)," *Journal of Applied Meteorology and Climatology*, Vol. 59, (5), 2020, pp. 885 – 899. DOI: 10.1175/JAMC-D-19-0161.1.

26. Mei, R., Luo, L.-S., and Shyy, W., "An Accurate Curved Boundary Treatment in the Lattice Boltzmann Method," *Journal of Computational Physics*, Vol. 155, (2), 1999, pp. 307–330. DOI: 10.1006/jcph.1999.6334.

27. Dorschner, B., Chikatamarla, S., Bösch, F., and Karlin, I., "Grad's approximation for moving and stationary walls in entropic lattice Boltzmann simulations," *Journal of Computational Physics*, Vol. 295, 2015, pp. 340–354. DOI: 10.1016/j.jcp.2015.04.017.

28. Ashok, S., and Rauleder, J., "Mid-fidelity NATO generic destroyer static and moving-ship airwake simulations using the Lattice-Boltzmann method compared with experimental data," *Ocean Engineering*, Vol. 298, 02 2024. DOI: 10.1016/j.oceaneng.2024.117264.

29. Wissocq, G., Gourdain, N., Malaspinas, O., and Eyssartier, A., "Regularized characteristic boundary conditions for the Lattice-Boltzmann methods at high Reynolds number flows," *Journal of Computational Physics*, Vol. 331, 2017, pp. 1–18. DOI: 10.1016/j.jcp.2016.11.037.

30. Kurban, E., Oates, B., Smith, M. J., and Rauleder, J., "Correlation of High- and Mid-Fidelity Ship Airwake Analysis to Experiment," *Journal of Aircraft*, 2025. DOI: 10.2514/1.C038087.

31. Wang, M., Feng, Y., Owen, D., and Qu, T., "A novel algorithm of immersed moving boundary scheme for fluid–particle interactions in DEM–LBM," *Computer Methods in Applied Mechanics and Engineering*, Vol. 346, 2019, pp. 109–125. DOI: 10.1016/j.cma.2018.12.001.

32. Aslan, E., Taymaz, I., and Benim, A. C., "Investigation of LBM curved boundary treatments for unsteady flows," *European Journal of Mechanics - B/Fluids*, Vol. 51, 2015, pp. 68–74. DOI: 10.1016/j.euromechflu.2015.01.004.

33. Sorensen, J. N., and Shen, W. Z., "Numerical Modeling of Wind Turbine Wakes," *Journal of Fluids Engineering*, Vol. 124, (2), 05 2002, pp. 393–399. DOI: 10.1115/1.1471361.

34. Apsley, D. D., Stallard, T., and Stansby, P. K., "Actuator-line CFD modelling of tidal-stream turbines in arrays," *Journal of Ocean Engineering and Marine Energy*, Vol. 4, (4), Nov 2018, pp. 259–271. DOI: 10.1007/s40722-018-0120-3.

35. Baba-Ahmadi, M. H., and Dong, P., "Validation of the actuator line method for simulating flow through a horizontal axis tidal stream turbine by comparison with measurements," *Renewable Energy*, Vol. 113, 2017, pp. 420–427. DOI: 10.1016/j.renene.2017.05.060.

36. Jha, P. K., and Schmitz, S., "Actuator curve embedding – an advanced actuator line model," *Journal of Fluid Mechanics*, Vol. 834, 2018, pp. R2. DOI: 10.1017/jfm.2017.793.

37. Churchfield, M. J., Schreck, S. J., Martinez, L. A., Meneveau, C., and Spalart, P. R., "An Advanced Actuator Line Method for Wind Energy Applications and Beyond," AIAA SciTech 35th Wind Energy Symposium, Grapevine, TX, 2017. DOI: 10.2514/6.2017-1998.

38. Asmuth, H., Olivares-Espinosa, H., Nilsson, K., and Ivanell, S., "The Actuator Line Model in Lattice Boltzmann Frameworks: Numerical Sensitivity and Computational Performance," *Journal of Physics: Conference Series*, Vol. 1256, 07 2019, pp. 012022. DOI: 10.1088/1742-6596/1256/1/012022.

39. Rullaud, S., Blondel, F., and Cathelain, M., "Actuator-Line Model in a Lattice Boltzmann Framework for Wind Turbine Simulations," *Journal of Physics: Conference Series*, Vol. 1037, 06 2018, pp. 022023. DOI: 10.1088/1742-6596/1037/2/022023.

40. Grondeau, M., Guillou, S., Mercier, P., and Poizot, E., "Wake of a Ducted Vertical Axis Tidal Turbine in Turbulent Flows, LBM Actuator-Line Approach," *Energies*, Vol. 12, (22), 2019. DOI: 10.3390/en12224273.

41. Bludau, J., Hajek, M., and Rauleder, J., "Solving the Ship-Rotorcraft Dynamic Interface Problem Using Lattice-Boltzmann Aerodynamics Two-Way Coupled with Blade Element Based Flight Dynamics," Proceedings of the Vertical Flight Society 77th Annual Forum, 05 2021. DOI: 10.4050/F-0077-2021-16725.

42. Gourdain, N., Singh, D., Jardin, T., and Prothin, S., "Analysis of the Turbulent Wake Generated by a Micro Air Vehicle Hovering near the Ground with a Lattice Boltzmann Method," *Journal of the American Helicopter Society*, Vol. 62, 10 2017. DOI: 10.4050/JAHS.62.042003.

43. Ashok, S. G., and Rauleder, J., "Real-Time Coupled Ship–Rotorcraft Interactional Simulations Using GPU-Accelerated Lattice-Boltzmann Method," *Journal of the American Helicopter Society*, Vol. 70, 2025, pp. 022005. DOI: 10.4050/JAHS.70.022005.

44. Wilhelm, S., Jacob, J., and Sagaut, P., "An explicit power-law-based wall model for lattice Boltzmann method–Reynolds-averaged numerical simulations of the flow around airfoils," *Physics of Fluids*, Vol. 30, June 2018, pp. 065111. DOI: 10.1063/1.5031764.

45. D'Humières, D., Ginzburg, I., Krafczyk, M., Lallemand, P., and Luo, L.-S., "Multiple-Relaxation-Time Lattice Boltzmann Models in Three Dimensions," *Philosophical transactions. Series A, Mathematical, physical, and engineering sciences*, Vol. 360, 04 2002, pp. 437–51. DOI: 10.1098/rsta.2001.0955.

46. Panigrahi, N., *Inverse Distance Weight*, Springer International Publishing, Dec 2021, p. 1–7. DOI: 10.1007/978-3-030-26050-7_166-1.

47. Werner, H., and Wengle, H., "Large-Eddy Simulation of Turbulent Flow Over and Around a Cube in a Plate Channel," *Turbulent Shear Flows 8*, edited by F. Durst, R. Friedrich, B. E. Launder, F. W. Schmidt, U. Schumann, and J. H. Whitelaw, Springer Berlin Heidelberg, Berlin, Heidelberg, 1993, pp. 155–168. DOI: 10.1007/978-3-642-77674-8_12.

48. Degrigny, J., Cai, S.-G., Boussuge, J.-F., and Sagaut, P., "Improved wall model treatment for aerodynamic flows in LBM," *Computers Fluids*, Vol. 227, 2021, pp. 105041. DOI: https://doi.org/10.1016/j.compfluid.2021.105041.

49. Jude, D., Hosseinverdi, S., Sitaraman, J., Peron, S., and Bolsard, R., “Actuator Line and Immersed Boundary Methods for Rotorcraft CFD,” Vertical Flight Society’s 80th Annual Forum & Technology Display, Montreal, Canada, May 2024. DOI: 10.4050/F-0080-2024-1128.

50. Wissink, A. M., Jude, D., Jayaraman, B., Roget, B., Lakshminarayan, V. K., Sitaraman, J., Bauer, A. C., Forsythe, J. R., and Trigg, R. D., “New Capabilities in CREATE-AV Helios Version 11,” AIAA Scitech 2021 Forum. DOI: 10.2514/6.2021-0235.

51. Nichols, R., and Buning, P., *User’s Manual for OVERFLOW 2.4*, NASA Langley Research Center, March 2024.

52. Wissink, A. M., Sitaraman, J., Jayaraman, B., Roget, B., Lakshminarayan, V. K., Potsdam, M. A., Jain, R., Bauer, A., and Strawn, R., “Recent Advancements in the Helios Rotorcraft Simulation Code,” 54th AIAA Aerospace Sciences Meeting. DOI: 10.2514/6.2016-0563.